Flow and Mass Transfer of Fully Resolved Bubbles in Non-Newtonian Fluids

Stefan Radl
Institute RNS, Graz University of Technology, Graz, Austria

Gretar Tryggvason
Dept. of Mechanical Engineering, Worcester Polytechnic Institute, Worcester, MA 01609

Johannes G. Khinast
Dept. of Chemical and Biochemical Engineering, Rutgers University, Piscataway, NJ 08845

DOI 10.1002/aic.11211
Published online June 5, 2007 in Wiley InterScience (www.interscience.wiley.com).

In this work, high-resolution 2-D numerical simulations were performed on the motion of deformable bubbles in non-Newtonian fluids and the associated mass transfer. For that purpose, we have implemented a semi-Lagrangian advection scheme and improved the fluid dynamic calculation by the usage of implicit algorithms. Non-Newtonian fluids are described by generalized Newtonian as well as viscoelastic model fluids. As shear-thinning model we use a Power-Law and a Carreau-Yasuda model, the viscoelastic fluid simulations are based on an Upper-Convected Maxwell model combined with a recently introduced model for the evolution of the effective shear rate. The mathematical challenges arising from the hyperbolic nature of the resulting set of equations are addressed by inclusion of artificial diffusion in the stress equation. In our work, it was found that shear thinning effects have impact on collision rates, and therefore, may influence coalescence of bubbles in non-Newtonian liquids. Furthermore, for the first time, concentration fields of dissolved gas in viscoelastic fluids are presented. The study shows that the fluid elasticity plays a major role for bubble rise velocity, and therefore, mass transfer. As the wake dynamics differ significantly from that in Newtonian liquids, abnormal mixing characteristics can be expected in the bubbly flow of viscoelastic fluids. © 2007 American Institute of Chemical Engineers *AIChE J,* 53: 1861–1878, 2007

Keywords: numerical simulation, bubbles, non-Newtonian liquids, mass transfer

Introduction

Because of persistent uncertainties in the underlying models and system properties, the scale-up of bioreactors remains a challenging problem. For example, the rheology of media in bioreactors is non-Newtonian in most cases.[1–8] However, details of the non-Newtonian fluid characteristics, such as viscoelasticity or the tendency for shear thinning, are frequently unknown or neglected. Furthermore, in contrast to Newtonian media, there is a lack of general correlations for mass and heat transfer rates, which are needed for the prediction of oxygen supply and heat removal. Similar observations can be made for the properties needed to precisely predict transport of metabolites, nutrients, or CO_2. So far, most studies are based on experimental investigations, which are usually interpreted with simple theoretical models.[3,4,8–11] First-

Correspondence concerning this article should be addressed to J. G. Khinast, currently Murie Curie Chair at the Institute RNS, Graz, at khinast@tugraz.at.

principles methods to predict mass-transfer coefficients, transport rates, and other parameters in non-Newtonian fluids have not been reported so far.

Local mass transfer is not the only micro-effect of central importance in the design of bioreactors. Knowledge of the localized forces, such as shear and normal stresses in the cell's microenvironment, is also a key for determining whether a bioreactor is suitable to handle sensitive biosystems.[12] Subcritical shear stresses found in the hydrodynamic environment of large-scale reactors may reduce cell productivity by impacting transcription, translation, secretion, and other mechanisms.[13] Even more importantly, serious damage to fragile microorganisms, biofilms, and immobilized biocatalysts due to high shear rates or normal forces has been reported.[14–20] However, it was shown recently that local stresses generated by agitation alone cannot cause significant cell lysis and necrosis.[21,22] Nevertheless, stresses encountered during bubble rupture at the free surface of the fermentation medium can lead to significant damage. Thus, cell attachment to rising bubbles would be critical to predict the rate of cell transport to the free surface and the ensuing damage rates (for an overview of the involved mechanism, refer to Nienow[23]). This has been the objective of numerous studies, both theoretically[24] as well as experimentally.[25] However, due to the complex interactions of surfactants, cells, and the bubbles, no ultimate model for the prediction of cell transport to the free surface is available at the moment.

In summary, there is a need to better understand the processes occurring on a microscale (bubble mass transfer, nutrient transport, cell attachment to rising bubbles, local stress distribution), since it is the (time-integrated) microenvironment of the cell which determines their productivity and life span. In the past, only a few publications addressed the effects in bioreactors on the microscale. For example, an analysis of cell stress due to local forces and hypoxia in Newtonian media has been reported by our group for the first time,[26,27] and the importance of accounting for both shear and normal forces, as well as the oxygen distribution, was illustrated. In another study by Richard and Margaritis[28] on the production of polyglutamic acid, the importance of predicting local shear rates and mass-transfer coefficients was pointed out. However, the authors did not develop micromodels to describe these effects.

To develop microscale models, it is critical to simulate the flow using model-free, first-principles tools, such as Direct Numerical Simulation (DNS) methods. With these methods it is now possible to fully resolve the interface of a bubble in all three dimensions and even to predict the interaction of many deformable bubbles.[29] The inclusion of species conservation, however, has been a persistent problem due to the high Schmidt numbers that require a large number of grid points to resolve the concentration field. For the first time, Koynov et al.[30] performed DNS of this challenging problem and provided detailed results on mass transfer and chemical reactions in fully deformable bubble swarms. The only significant restriction of their work is the use of a 2-D rectangular grid, which is also used in the current work.

In this contribution, we extend their method to realistic non-Newtonian media, including viscoelastic fluids, to precisely study and predict effects encountered in biotechnological applications. We apply the method to gassed bioreaction systems, where the liquid phase is continuous and bubbles are rising in a non-Newtonian fluid. Different scenarios are considered, such as purely viscous fluids and viscoelastic media, whose rheology is described by an Upper-Convected Maxwell (UCM) model fluid. To the best of our knowledge, this is the first report of first-principles simulations of mass transfer around bubble swarms in non-Newtonian fluids, including viscoelastic media. Using our method it will be possible to compute mass-transfer coefficients, shear and elongation rate distributions, and other parameters in non-Newtonian fluids, without any experimental data or correlations.

Background

Gas–liquid mass transfer and species transport in chemical and bioreactors have been investigated for many decades as a basis for rational design, operation, and scale-up of these reactors. In most studies, experimental methods that assume a perfectly mixed batch reactor were used.[11,31,32] This technique is based on the measurement of the time evolution of the average dissolved gas concentration in the reactor. With this approach, only the product of liquid-phase mass-transfer coefficient k_l and the specific interface area a, i.e., the volumetric mass-transfer coefficient $k_l a$, can be estimated. Based on these data, dimensionless correlations for the modified Sherwood number Sh* as a function of the Reynolds number Re, the Schmidt number Sc, and the Froude number Fr can be developed. In the case of non-Newtonian fluids, the apparent viscosity μ_{ap} and an averaged shear rate $\dot{\gamma}_{ap}$ are used in the $Sh = f(Re, Sc, Fr)$ correlations.[7] More refined experimental techniques include estimation of the influence of the flow index n of the power-law shear-thinning model.[9,33]

However, for typical biotechnological applications (e.g., viscoelastic xanthan gum suspensions) the mass-transfer coefficient is significantly underestimated using this approach. This is due to the exclusion of the fluid elasticity, which can be a significant factor in bioreactor broths.[9,33]

In the last years, there has been increased interest in understanding mass transport and mixing in gas–liquid multiphase systems using computational methods. One approach focuses on the large-scale mixing pattern in the reactor. Clearly, in such macroscale simulations, neither the hydrodynamics nor the concentration fields can be fully resolved. Only averaged quantities are obtained, and models for the drag, mass-transfer coefficients, and turbulence closures need to be provided. To model the turbulence, most simulations of the continuous phases have been based on Reynolds-averaged Navier Stokes (RANS) equations[34–36] and large eddy simulations (LES).[37–42] The literature concerning such macroscale approaches is extensive[37,43] and includes either Euler-Euler or Euler-Lagrangian methods. In Euler-Euler simulations, the multiphase system is treated as two interpenetrating continuous phases. In Euler-Lagrange simulations, the multiphase system is modeled as a continuous phase, in which the disperse phase is tracked and treated as point source for mass and momentum exchange.

The second approach focuses on microscale simulations, entailing a full resolution of all effects on all scales and, thus, obviating the need of any subgrid modeling. The detailed knowledge of micro-effects can then be used to test

closures for macroscale simulations.[44] For example, Koynov et al.[30] studied mass transfer from single and multiple bubbles rising in a quiescent liquid. In their simulation no mass-transfer correlations were needed. Instead, mass-transfer coefficients were predicted, which agreed very well with experimental literature data. Such simulations are called DNS, because the hydrodynamics as well as the concentration fields result directly from first principles. However, the computational mesh has to be fine enough, such that the Kolmogorov length scale η (turbulence) and the Batchelor length scale η_B (concentration field) can be resolved:

$$\frac{\eta}{l_0} \approx \mathrm{Re}^{-3/4} \tag{1}$$

$$\eta_B \approx \eta \cdot \mathrm{Sc}^{-1/2} \tag{2}$$

In liquids the Batchelor scale is about 20–100 times smaller than the Kolmogorov scale, since liquid-phase Schmidt numbers typically vary between 500 and 10,000. In addition to the length-scale, also the smallest time scales of the chemical reactions and the fluid dynamics have to be resolved. Therefore, the computational requirements of DNS of reacting flows in liquids are much higher than purely fluid dynamical calculations. As a consequence, DNS of reacting systems is limited to low Re-number problems or to 2-D cases.

For the DNS of multiphase systems with fully resolved interfaces, different techniques have been used. The first approach includes front capturing methods, where the front is captured directly on a uniform grid. The volume of fluid method is a typical example and has been used widely.[45,46] Lagrangian methods, in which the grid follows the fluid, have been reported.[47] The Lagrangian approach was coupled with an unstructured, moving finite-element mesh by Hu et al.[48] to simulate the movement of particles. A third method by Leal and coworkers uses separate grids for each phase and can thus provide very high accuracy.[49,50] Unfortunately, only simple geometries can be described. Another approach is the front-tracking (FT) method,[29,51] where a separate grid is used to track the front, whereas the conservation equations are solved on a fixed uniform grid. With such methods, very high accuracy, even for complex flows, can be achieved.[52]

In most recent CFD simulations of multiphase and bioreactors it was assumed that the liquid phase is a Newtonian fluid, although it is known from numerous experimental studies that the rheology is often strongly non-Newtonian.[1–9,11] When non-Newtonian behavior was considered, generalized Newtonian-fluid models (GNFMs) were employed, where the fluid is assumed to exhibit only viscous effects. With GNFMs it is possible to use the same framework as for Newtonian fluids. The constant viscosity is hereby replaced by a viscosity that is a function of the local shear rate. However, experiments suggest that most non-Newtonian fluids, such as fermentation broths or cell suspensions, exhibit elastic effects that pose significant challenges for the numerical implementation. To describe their rheology, linear and nonlinear viscoelastic models have been proposed. The most straightforward linear viscoelastic fluid model is the Maxwell model. It has many modifications and the upper-convected version (the UCM-model) has been used successfully in CFD-codes to describe viscoelastic fluid behavior. It is based on the serial combination of viscous components via viscous dampers (characterized by the viscosity μ) and linear elastic contributions via Hookean springs (characterized by the constant K_{Spring}). Nonlinear viscoelastic models, such as the Oldroyd-B, Giesekus, or Phan-Thien & Tanner (PTT) models, can be derived from the Maxwell model or from molecular theory. Such models are mostly applied to polymer melts and solutions, where polymer molecules are described as beads connected with spring elements (e.g., FENE-type models). Nevertheless, development of models for non-Newtonian fluids is still an ongoing process. A complication of viscoelastic CFD simulations is the fact the equations governing the flow become hyperbolic in nature, giving rise to additional problems when trying to solve the equations numerically. Thus, CFD algorithms for viscoelastic fluid simulations need to be significantly more sophisticated and stable.

The difficulties of viscoelastic fluid simulations have been summarized as the "high-Weissenberg number problem (HWNP)." The Weissenberg number (Wi) is the ratio of a characteristic elastic time (relaxation time t_m) and a characteristic time of the flow. Simulations are limited to a maximal attainable Wi-number, depending on the algorithm. When the elasticity of the fluid dominates the viscous effects, CFD simulations begin to become unstable. Despite several approaches to solve this problem, the HWNP remains somewhat of a mystery,[53–61] and the fundamental question, whether the limiting Wi-number is a purely numerical phenomenon or rather a breakdown of the constitutive equations, is still under debate.

Using classical methods like the elastic-viscous-split-stress (EVSS) formulation and its modifications, the simulation of viscoelastic fluids is restricted to Wi-numbers in the order of O(1) for the flow past a cylinder. Recently, there have been attempts to overcome this problem using a transformation to logarithmic variables together with a discrete elastic-viscous-split-stress (DEVSS) formulation.[62] These attempts are successful in the sense that a limiting Wi-number does not exist anymore for the Giesekus model. This example illustrates that the simulation of viscoelastic fluids, even for simple constitutive equations such as the Oldroyd-B or UCM model, is still a challenge.

The sedimentation of a sphere in an elastic fluid has become a benchmark problem in non-Newtonian fluid mechanics.[63] Typical features of this flow in comparison to the Newtonian case can be observed. Experiments (for a review refer to McKinley[63]) and numerical simulations[64,65] have confirmed the existence of a "negative wake," i.e., an additional recirculating region downstream of the sphere with a reversed vorticity compared to the motion near the sphere. This flow structure is very sensitive to the relative magnitude of the shear-thinning (pseudoplasticity) and the elastic effects. Similar phenomena are observed for the flow of bubbles in non-Newtonian liquids,[66,67] leading to teardrop-shaped bubbles. It is believed that both effects (shear-thinning and viscoelasticity) are responsible for this atypical behavior of bubbles in non-Newtonian liquids.[63] Another effect that has been observed in viscoelastic fluids is the jump discontinuity of the bubble's rise velocity.[66,68–70] Herrera-Velarde et al.[70] found that the velocity field around the

bubble changes abruptly for bubble volumes at a critical value. In addition, they reported an influence of the container size on the magnitude of the jump discontinuity.

In summary, there are significant efforts to investigate gas–liquid flows in non-Newtonian liquids, including viscoelastic media. In contrast, there have been no studies in the literature addressing mass transfer, chemical reactions, and the dynamics of bubble swarms in such liquids based on high-fidelity computations. However, a detailed understanding of bubble dynamics, (bio)chemical reactions, species transport, and mass transfer is critical for the design, operation, and scale-up of many industrially relevant systems, such as cell-culture bioreactors and fermentors. Mammalian cell cultures (e.g., CHO cells for therapeutic proteins production) and filamentous fungi fermentors (production of antiinfectives and vaccines) are known to be persistently hard to scale-up. For such systems a detailed understanding of the local microphenomena, which are the ones determining cell stress and viability, is important and will open the door to much improved systems with higher productivity and stability.

To address such problems, we present a new DNS method to investigate all relevant effects in bubble swarms in non-Newtonian media, including the dynamics of bubble swarms, the deformation of bubbles, species transport, and mass transfer between bubbles and liquid phase. These results may help to develop and to test microscale models, e.g., for gas–liquid mass transfer, which can be used subsequently for macroscale CFD simulations.

Problem Formulation

In our work, a modified 2-D hybrid FT/front-capturing method[29] is used to simulate the motion of deformable gas bubbles in non-Newtonian liquids, including the solution of the species conservation equation. We fully resolve the fluid dynamics as well as the concentration field around individual bubbles on a grid containing almost 7 million nodes. This approach allows us to predict accurately bubble dynamics as well as mass-transfer coefficients. The basics of the computational method are described in Koynov et al.[30] The focus of this work is our new scheme for the solution of the species conservation equations and the implementation of purely viscous and viscoelastic non-Newtonian fluid models.

Fluid dynamics

In the FT/front-capturing method, the front of the bubble is directly tracked and the material properties, such as density, viscosity, and diffusivity, can then be reconstructed on a fixed grid. The jump in the material properties as well as the interfacial momentum exchange at the phase boundary is directly captured that way. Therefore, no additional modeling is required. Finally, the momentum balance and the species conservation equation are solved in the entire domain, treating the multiphase system as a single fluid with changing material properties.

The dimensionless groups governing the non-Newtonian bubble flow are (i) the Morton number, $\mathrm{Mo} = g \cdot \mu_l^4 \cdot \Delta\rho / (\rho_l^2 \cdot \sigma^3)$, (ii) the Eötvös number, $\mathrm{Eo} = g \cdot \Delta\rho \cdot d_b^2/\sigma$, (iii) the Deborah number $\mathrm{De} = t_m \cdot U_t/d_b$ in the case of the viscoelastic fluids, where t_m is the relaxation time of the fluid, and (iv) the dimensionless model parameters of the shear thinning model for purely viscous non-Newtonian media. The Reynolds (Re) number $\mathrm{Re} = d_b \cdot U_t \cdot \rho_l/\mu_l$ is a result of simulations. In the case of power-law shear-thinning fluids, the Re number was calculated with the representative shear rate to give $\mathrm{Re}_{\text{power-law}} = d_b^n \cdot U_t^{(2-n)} \cdot \rho_l/K$.

Purely Viscous Fluids. In the case of purely viscous fluids, the governing equations can be written as

$$\frac{\partial \rho \cdot \vec{u}}{\partial t} + (\vec{u} \cdot \nabla)\rho\vec{u} = -\nabla p + \rho \cdot \vec{f} + \nabla \cdot \left[\mu(\vec{x}) \cdot \left(\nabla\vec{u} + \nabla^{\mathrm{T}}\vec{u}\right)\right] + \oint \sigma\kappa'\vec{n}' \cdot \delta^2 \cdot (\vec{x} - \vec{x}')\cdot ds' \quad (3)$$

$$\nabla \cdot \vec{u} = 0. \quad (4)$$

These equations are satisfied for the entire computational domain, regardless of the discontinuities in the material properties.[29] As we need the local shear rate (Eq. 5) for the reconstruction of the viscosity, the latter is calculated with a central differences scheme from the velocity field $\vec{u}$ via the rate-of-deformation tensor D (Eq. 6).

$$\dot{\gamma} = \sqrt{2 \cdot D : D} \quad (5)$$

$$D = \frac{1}{2} \cdot \left(\nabla\vec{u} + \nabla^{\mathrm{T}}\vec{u}\right) \quad (6)$$

Viscoelastic Fluids. In the case of a viscoelastic fluid, the momentum equation is solved in the form:

$$\frac{\partial \rho \cdot \vec{u}}{\partial t} + (\vec{u} \cdot \nabla)\rho\vec{u} = -\nabla p + \rho \cdot \vec{f} + \nabla \cdot \tau + \oint \sigma\kappa'\vec{n}' \cdot \delta^2 \cdot (\vec{x} - \vec{x}')\cdot ds' \quad (7)$$

together with the continuity equation (Eq. 4). For this case, the stress tensor τ is computed explicitly.

Constitutive equations for non-newtonian fluids

Purely Viscous Fluid Models. For viscous non-Newtonian fluids, we use a power law model (Eq. 8) and a Carreau-Yasuda shear-thinning model (Eq. 9).

$$\mu(\vec{x}) = K \cdot \dot{\gamma}(\vec{x})^{n-1} \quad (8)$$

$$\frac{\mu(\vec{x}) - \mu_\infty}{\mu_0 - \mu_\infty} = \left[1 + (\lambda \cdot \dot{\gamma}(\vec{x}))^a\right]^{\frac{n_{\mathrm{CY}}-1}{a}}, \quad (9)$$

K denotes the consistency index in $\mathrm{Pa} \cdot \mathrm{s}^n$, and n is the flow index of the power law model. In the Carreau-Yasuda model, μ_∞ and μ_0 denote the shear viscosity at infinite and zero shear rate, respectively. λ, a, and n_{CY} are dimensionless parameters.

Once the local shear rate has been calculated at each nodal point of the domain, the apparent viscosity can be reconstructed, as the local viscosity changes instantaneously with the shear rate. In the presented examples the power law model with a low shear-rate cutoff was used. However, any

other model on the basis of a generalized Newtonian fluid can be used.

Viscoelastic Fluid Models. For viscoelastic media the UCM fluid model has been implemented, which allows inclusion of elastic effects, at least qualitatively. The model can be refined using a full relaxation spectrum. However, the following description is based on a single-mode UCM fluid model for simplicity (Eq. 10).

$$\tau(\vec{x},t) + t_{\mathrm{m}} \cdot \overset{\nabla}{\tau}(\vec{x},t) = 2\mu(\vec{x},t) \cdot D \tag{10}$$

Here t_{m} denotes the relaxation time of the fluid and D is the rate-of-strain tensor. Due to the shear-thinning effects of the viscosity μ and due to the upper-convected derivative $\overset{\nabla}{\tau}(\vec{x},t)$ in Eq. 11,

$$\overset{\nabla}{\tau}(\vec{x},t) = \frac{\partial \tau(\vec{x},t)}{\partial t} + \vec{u} \cdot \nabla\tau(\vec{x},t) - \nabla\vec{u} \cdot \tau(\vec{x},t) - \tau(\vec{x},t) \cdot \nabla^{\mathrm{T}}\vec{u}, \tag{11}$$

even the single-mode UCM fluid model is a nonlinear viscoelastic model. The nonlinearity is introduced by the last two terms in the upper-convected derivative (Eq. 11) that represent the deformation of the coordinate system in which the stresses are calculated.[71] This formulation results in a set of 2-D partial differential equations for each stress component of the tensor τ.

The relaxation time t_{m} in the case of a single-mode Maxwell model is established from an experimentally determined relaxation function $G(s)$, which is defined as (for the derivation refer to Böhme[71]):

$$G(s) = G_0 \cdot \exp\left[-\frac{s}{t_{\mathrm{m}}}\right], \tag{12}$$

where s denotes the time. Experiments are usually designed to determine the complete spectrum of relaxation times $t_{\mathrm{m},k}$. Thus, the relaxation function $G(s)$ can be approximated by a discrete spectrum, i.e.,

$$G(s) = \sum_{k=1}^{K} G_k \cdot \exp\left[-\frac{s}{t_{\mathrm{m},k}}\right]. \tag{13}$$

The constitutive equation then becomes[71]

$$\tau_k(\vec{x},t) + t_{\mathrm{m},k} \cdot \overset{\nabla}{\tau_k}(\vec{x},t) = 2\mu_k(\vec{x},t) \cdot D \tag{14}$$

$$\tau = \sum_{k=1}^{K} \tau_k(\vec{x},t), \tag{15}$$

where viscosity μ_k can be calculated as

$$\mu_k = t_{\mathrm{m},k} \cdot G_k. \tag{16}$$

Thus, for each mode the UCM model has to be solved, and the arising stresses corresponding to each mode have to be summed up. In our simulations, a single-mode UCM model has been used in order to save computational resources. However, multimode simulations can be easily implemented.

Such multimode simulations were carried out by Frank and Li[64] and Kemiha et al.[65] with some modifications. First, they used a simple Maxwell model instead of considering the upper-convected derivative. Secondly, they used a modification of the relaxation times to account for shear-thinning effects. This approach has the advantage that the data obtained by standard rheological characterization methods can be used, and only two additional parameters, i.e., the characteristic time $t_{\mathrm{r},0}$ for the time-delay of the relaxation time and a reference shear rate ϕ_0, have to be estimated.

A similar approach was used in our study, but only for the shear-thinning effect. Like Kemiha et al.,[65] we use a Carreau model for the interdependence between viscosity and an "effective" shear rate ϕ. Thus, the viscosity is calculated (Eq. 17) using the value ϕ as a characteristic shear rate instead of the physical shear rate $\dot{\gamma}$ determined by the actual velocity field. The quantity ϕ is described by a simple ODE (Eq. 18) with two new parameters $t_{\mathrm{r}0}$ and ϕ_0 (Eq. 19).

$$\frac{\mu(\phi) - \mu_\infty}{\mu_0 - \mu_\infty} = \left[1 + (\lambda \cdot \phi)^2\right]^{(n-1)/2} \tag{17}$$

$$\frac{\partial \phi}{\partial t} = -\frac{\phi - \dot{\gamma}}{t_{\mathrm{r}}(\phi)} \tag{18}$$

$$t_{\mathrm{r}}(\phi) = \frac{t_{\mathrm{r},0}}{1 + (\phi/\phi_0)} \tag{19}$$

The viscosity is equal to the value calculated from the Carreau model, when the effective shear rate ϕ approaches the physical shear rate $\dot{\gamma}$. As the parameters $t_{\mathrm{r},0}$ and ϕ_0 cannot be determined using standard rheological methods (e.g., oscillation experiments in rotational viscosimeters), Frank and Li[64] used consecutive relaxation experiments to estimate these values. They proposed the values of $t_{\mathrm{r},0} = 12$ (s) and $\phi_0 = 0.50$ (s^{-1}) for their 0.5% polyacrylamide solution. The same parameters were used in our study.

Species conservation equation

The equation describing the transport of species α is

$$\frac{\partial c_\alpha}{\partial t} + (\vec{u} \cdot \nabla)c_\alpha = D_\alpha \cdot \nabla^2 c_\alpha + \sum_j \nu_{\alpha,j} \cdot r_j. \tag{20}$$

Note that as we fully resolve the concentration field, D_α is the true molecular diffusion coefficient. The Schmidt number, $\mathrm{Sc} = \mu_{\mathrm{l}}/\rho_{\mathrm{l}}\, D_\alpha$, is the dimensionless number characterizing the viscous momentum transport in relation to the diffusivity of species α. The last term in Eq. 20 is the chemical reaction term.

Numerics

In general, the model can be solved using methods for single-phase system, since a priori both phases are treated as one fluid, with the physical properties changing at the interface. Unless otherwise stated, we use a central-differences discretization on a fixed, rectangular, staggered grid. The interface is marked with a separate 1-D grid that is advected with the computed velocity field.

Integration of the momentum equation

The momentum and the mass conservation equations are solved simultaneously for the time step $n + 1$ in the compu-

tational domain, using a two-step method.[30] In the first step (prediction step), the pressure gradient in the momentum equations is neglected, and an intermediate velocity field u^* is computed. Since the emphasis of this study is bubble motion in non-Newtonian fluids that are often highly viscous, stability of the simulation at low Re-numbers is important. For explicit formulations the time-step criterion from the viscous term in the momentum equations is

$$\Delta t_{\max,\mathrm{visc}} = \frac{1}{4} \cdot \frac{(\Delta x)^2}{\max\left(\frac{\mu_1}{\rho_1}, \frac{\mu_2}{\rho_2}\right)}, \tag{21}$$

where the indices 1 and 2 denote the two phases. As can be seen, the maximum time-step size is decreasing with increasing viscosity and decreasing grid-width. To relax this constraint for highly viscous flows, a Crank-Nicholson (CN) Scheme was used to obtain a second-order accurate time stepping, i.e.,

$$\frac{\rho^{n+1} \cdot \vec{u}^* - \rho^n \cdot \vec{u}^n}{\Delta t} = -(\nabla_h \cdot \vec{u}^n)\rho^n \vec{u}^n + \nabla_h \cdot \left[\mu^n(\vec{x}) \cdot \frac{1}{2} \cdot \left(\nabla_h \vec{u}^n + \nabla_h \vec{u}^* + \nabla_h^{\mathrm{T}} \vec{u}^n + \nabla_h^{\mathrm{T}} \vec{u}^*\right)\right] + \vec{F}_\sigma. \tag{22}$$

In Eq. 22 the subscript h denotes the numerical approximation of the spatial derivative and "*" refers to the preliminary velocity field at time step $n + 1$. In the case of a viscoelastic fluid model, the viscous term on the right-hand side of Eq. 22 is replaced by the total stress term. The viscous part of the stress term is still considered implicitly (i.e., the average between time step "n" and "*" is used), leading to improved stability. Due to the spatially varying viscosity, a mixed derivative appears in the expression for the viscosity term in the discretized momentum equation (Eq. 22). This term was considered explicitly. With this formulation formally no stability criterion has to be satisfied in contrast to Koynov et al.[30] Thus, the current version of the code is significantly faster. To reduce the computational effort, an alternating direction implicit (ADI) scheme was used, such that only a tridiagonal system needs to be solved in each direction.

In the second step, the pressure gradient is added resulting in a Poisson-like equation that is solved via an SOR algorithm. The use of an iterative method (instead of a fast Poisson solver) is necessary due to the variable density.[29,30]

Discretization of the viscoelastic constitutive equation

The solution procedure used in our work is based on the method of Sarkar and Schowalter.[72] The constitutive equations (Eqs. 10 and 11) can be rearranged to yield

$$\tau(\vec{x},t) + t_{\mathrm{m}} \cdot \frac{\partial \tau(\vec{x},t)}{\partial t} = K(\vec{x},t). \tag{23}$$

The tensor K on the right-hand side of Eq. 23 is

$$K(\vec{x},t) = 2\mu(\vec{x},t) \cdot D - t_{\mathrm{m}} \cdot \left[\vec{u} \cdot \nabla\tau(\vec{x},t) - \nabla\vec{u} \cdot \tau(\vec{x},t) - \tau(\vec{x},t) \cdot \nabla^{\mathrm{T}}\vec{u}\right]. \tag{24}$$

Each stress component of K can be integrated by parts to give the following discretized form:

$$\tau^{n+1}(\vec{x},t) - \tau^n(\vec{x},t) \cdot \exp\left[-\Delta t/t_{\mathrm{m}}\right] = K^{n+1}(\vec{x},t) - K^n(\vec{x},t) \cdot \exp\left[-\Delta t/t_{\mathrm{m}}\right] - \int_{t^n}^{t^{n+1}} \exp\left[-t/t_{\mathrm{m}}\right] \cdot \frac{\partial K(\vec{x},t)}{\partial t} \cdot dt \tag{25}$$

By neglecting variations of $K(\vec{x},t)$ with time, the integral in Eq. 25 can be omitted. Furthermore, this implies that $K^{n+1}(\vec{x},t)$ is equal to $K^n(\vec{x},t)$ and the following explicit numerical scheme for the calculation of the new stresses at the time step t^{n+1} is obtained:

$$\tau^{n+1}(\vec{x},t) = \tau^n(\vec{x},t) \cdot \exp\left[-\Delta t/t_{\mathrm{m}}\right] + K^n(\vec{x},t) \cdot \left(1 - \exp\left[-\Delta t/t_{\mathrm{m}}\right]\right). \tag{26}$$

Note that in this scheme no singularity exists for relaxation times t_{m} approaching zero, which is the case inside the bubble. As noted by Sarkar and Schowalter,[72] another advantage of this method is that the elliptic nature of the equations is retained, and no additional problems occur associated with the hyperbolic nature of Eq. 23. This effect could not be confirmed in our work. However, two problems have been reported by Sarkar and Schowalter[72]: first, for the convective terms in the stress equation a central-differencing scheme is not stable. Thus, a second-order QUICK scheme was used by them. In our code the convective stress terms in Eq. 24 are computed based on a SMART-bounded-QUICK scheme[73] to minimize stress overshoots and spurious oscillations in the stress field. Secondly, choice of the initial and boundary conditions is critical for the simulations. For a detailed discussion regarding the implementation of boundary conditions in the current work refer to Appendix A.

Artificial diffusion to stabilize the constitutive equation for viscoelastic fluids

Introduction of artificial diffusion (AD) into hyperbolic equations is a common way to stabilize this type of mathematical problem. The diffusion term hereby acts as a sink for spurious oscillations in the stress field. Furthermore, in our simulation the relaxation time has a jump at the gas–liquid interface, leading to additional perturbations. AD stabilization has been used in viscoelastic fluid simulations, e.g., for Oldroy-B fluids, and the algorithm's stability and the effect on the dynamics of time-dependent viscoelastic flows have been assessed by different authors.[74,75] Their procedure is based on an implicit form of the AD term in the stress equation. In our code the diffusion term is added in the Crank-Nicholson method directly to the intermediate stress tensor $\tilde{\vec{\tau}}^{n+1}$ calculated from the constitutive equation.

$$\vec{\tau}^{n+1} = \tilde{\vec{\tau}}^{n+1} + \kappa \cdot \Delta t \cdot \left(\frac{\nabla^2 \vec{\tau}^n}{2} + \frac{\nabla^2 \vec{\tau}^{n+1}}{2}\right) \tag{27}$$

This equation (Eq. 27, a Helmholtz PDE) is then solved for the new stresses $\vec{\tau}^{n+1}$ at each nodal point. It was shown by Sureshkumar and Beris[74] that if the length scale of the stress diffusivity is small compared to the length scale of the

smallest eddies, the simulation can be stabilized, without disrupting the qualitative behavior of the flow. The length scale associated with the stress diffusion term is

$$l_\kappa/h = \sqrt{\kappa \cdot \mathrm{Wi}}, \tag{28}$$

where Wi is the Weissenberg number, h is a reference length, and κ is the dimensionless artificial stress diffusivity. As the length scale of the smallest viscous eddies is $l_\mu/h = \sqrt{1/\mathrm{Re}}$, the ratio between the length at which stress fluctuations are damped and the smallest viscous eddies is

$$l_\kappa/l_\mu = \sqrt{\kappa \cdot \mathrm{Re} \cdot \mathrm{Wi}}. \tag{29}$$

Sureshkumar and Beris[74] used values of κ from 10^{-2} to 10^{-4} in their simulation of turbulent flows in a pipe (Re = 5000 and We = O(1)), resulting in values of l_κ/l_μ between 0.7 and 7, which is unsatisfactory. They concluded that a finer mesh is needed for lower values of κ. However, in our study the aim is to predict the mass transfer in laminar flow with Re-numbers of O(10) and a Wi-number of O(1). As we use artificial stress diffusivities in the order of 10^{-2} to 10^{-4}, the length scale of the stress diffusivity will be small compared to the scale of the smallest eddies. Thus, the behavior of the flow can be conserved when applying the artificial stress diffusion algorithm for stabilization.

Semi-Lagrangian advection for the species conservation equation

Since the Pèclet numbers of our problems are high (1000–10,000 for the flow of air bubbles in water), the advection term is dominating the diffusion term. Therefore, use of an accurate advection scheme producing no or an insignificant amount of numerical diffusion is critical for the resolution of the steep gradients. The solution of the species conservation equation with direct, first-order discretization (variations of the upwind scheme) typically leads to inaccurate results due to numerical diffusion, introduced by the discretization of the convection term. Thus, in our simulation a novel semi-Lagrangian (SL) advection scheme is used that was initially developed for atmospheric modeling.[76] This scheme is very stable (high Courant-numbers are feasible), accurate (about one order of magnitude better than the conventional advection schemes), and it is relatively straightforward to implement in comparison to an operator combined SL (OC-SL) scheme (see Staniforth and Côté[76]). Our operator splitting – SL – scheme first advects the concentration field directly from the departure point to the current grid point. Then, the algorithm carries out the diffusion and reaction step.

Step 1: Advection with a Semi-Lagrangian Scheme. In this step the following 2D-advection problem is solved

$$\frac{dc_\alpha}{dt} = \frac{\partial c_\alpha}{\partial t} + u \cdot \frac{\partial c_\alpha}{\partial x} + v \cdot \frac{\partial c_\alpha}{\partial y} = 0. \tag{30}$$

The discretized form of this equation is[76]

$$\frac{c_\alpha^+ - c_\alpha^-}{2 \cdot \Delta t} = 0. \tag{31}$$

In this centered $O(\Delta t^2)$ approximation the index "+" denotes values at the arrival point (on the grid) and the index "–" the quantities at the departure point. Clearly, $c_\alpha^+ = c_\alpha^-$. To compute the unknown concentration at the departure point, it is necessary to know the concentration field $c_\alpha(\vec{x}, t^{n-1})$ at $t - \Delta t$.

The sub-steps of this scheme are:

- Determination of the distance vector $\vec{\alpha}$ between arrival and departure point. For this, an iteration cycle was implemented, where an initial value of the distance vector is estimated, and then the pathway of an imaginary particle at the considered grid node is tracked half a step backwards. At this intermediate position the velocity is interpolated bilinearly to get the new distance vector $\vec{\alpha}$. This procedure is repeated three times, which is sufficient for convergence.
- Computation of the coordinates of the departure point $\vec{x}_{\mathrm{dep}} = \vec{x} - 2 \cdot \vec{\alpha}$
- Interpolation of the concentration c_α^- at the departure point $\vec{x}_{\mathrm{dep}}$ by interpolation between the grid values. An adaptive bicubic interpolation at $t - \Delta t$ is used, as described in Staniforth and Côté.[76] The choice of the interpolation method used is critical, because over- and undershoots must be avoided at any time. As the interpolation scheme is quite slow, in our algorithm it is skipped in areas where the concentration is under a certain limit.
- Set $c_\alpha^+ = c_\alpha^{n'} = c_\alpha^-$

Step 2: Diffusion with a Crank-Nicholson Scheme. A standard implicit CN-Scheme is used together with an ADI algorithm to reduce the computational cost.

The new semi-Lagrangian algorithm has two main advantages:

- Advection is based on a semi-Lagrangian scheme and is therefore much more stable. In contrast to conventional advection schemes used in other studies, the SLCN-scheme does not need to satisfy any stability criterion. Thus, any time step will result in a stable calculation. However, since the linear SL-scheme is only second-order accurate, it is suggested to limit the dimensionless time step to a Courant number α of 4–5.[77]
- The scheme is highly accurate, even at high Peclet-Numbers (Pe). Thus, even steep gradients in the flow field and in the concentration boundary layer may be resolved.

Another criterion for time steps necessary to obtain accurate simulations is to resolve a minimum relative wavelength.[77] However, this criterion was always satisfied in our computations due to the low diffusivities.

Simulation parameters

The dimensions of the computational domain used was $6d_b \times 18d_b$ for most simulations of viscoelastic fluids and $12d_b \times 36d_b$ for other simulations. Periodic boundary conditions were used at all sides of the rectangular computational domain. Due to stability problems in the solution of the momentum equation, the density ratio of gas and liquid phase was 1:10. Since the magnitude of gas-liquid interactions depends on the difference in density and not the ratio, this will not cause significant deviation in the results. The sensitivity of the results with respect to the density and viscosity ratio is discussed in Appendix B.

The time step size was set to 1–4 times of the maximum stable viscous time step $\Delta t_{\mathrm{max,visc}}$ (Eq. 21) depending on the

desired level of accuracy. Furthermore, the restriction due to the advection term at high Reynolds-numbers

$$\Delta t_{\mathrm{adv}} = 2 \cdot \frac{\min\left(\frac{\mu_1}{\rho_1}, \frac{\mu_2}{\rho_2}\right)}{V_{\max}^2} \tag{32}$$

and the Courant criterion ($\alpha = 4$) were checked. If necessary, the time step was decreased accordingly. For simulations involving viscoelastic fluids an even smaller time step had to be used to guarantee stability.

The grid resolution for the fluid dynamical computations was chosen depending on the bubble Re number and was varied between 120 × 360 and 200 × 600 cells such that the smallest scales were resolved and the fluctuation of bubble volume were acceptable (i.e., less than 1%). Solution of the species conservation equations were done on a finer grid. The grid resolution used was adjusted between 500 × 1500 and 1500 × 4500 cells to resolve the concentration boundary layer at high Pe numbers. With this grid, a maximum Schmidt number of 400 and Peclèt number of 2000 could be considered. This illustrates that a 3-D DNS with fully resolved boundary layer at realistic Schmidt and Peclet number is only possible with parallel machines using more than 10^9 grid points.

Results

The implemented Crank-Nicholson scheme enabled us to reduce the computational cost at low Re-numbers by about 90% compared to the older version of Koynov et al.[30] The CN scheme improved the stability of the non-Newtonian fluid simulations, enabling us to carry out simulations with a low power-law index (strongly shear-thinning fluids). Furthermore, the SL-advection scheme proved to result in low numerical diffusion. Thus, we were able to fully resolve the concentration boundary layer close to the bubble interface as shown in Figure 1. Thus, with our code even high Schmidt-number problems can be simulated. The computational cost of this scheme, i.e., the adaptive bicubic interpolation at the departure point, was mostly absorbed by an adaptive algorithm that skips points where advection terms can be neglected.

Validation of the numerical algorithm and the models

Extensive tests of the semi-Lagrangian advection scheme and the diffusion step were conducted to validate and demonstrate the accuracy of the scheme. Tests were conducted on a 500 × 500 and a 1000 × 1000 grid to investigate the grid dependence of the solution. The setup consisted of a spherical bubble (diameter d_b, no buoyancy forces) in a $12d_b \times 12d_b$ domain, in which diffusion and advection was simulated. In order to test the advection scheme, the liquid surrounding the bubble was advected with a certain velocity. The bubble had the same velocity. Thus, the situation imitates a stagnant bubble were mass transfer is only due to diffusion. As the thickness of the concentration boundary layer is not affected by the velocity field in this test case, a 500 × 500 grid was sufficient to accurately approximate the concentration field. The results were compared to the solution for the diffusion around a cylinder, as shown in Figure 1, and the agreement is excellent.

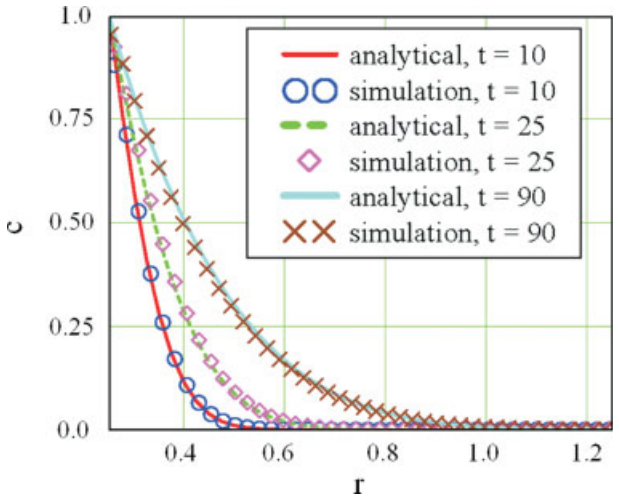

Figure 1. Concentration profile for test case.

Line: analytical solution; circle/diamond/cross: numerical values; resolution: 500 × 500, $D = 5.13 \times 10^{-4}$, $t_{\max} = 90$, $\Delta t = 0.2$). [Color figure can be viewed in the online issue, which is available at www.interscience.wiley.com.]

To obtain a grid-independent solution in the production runs, a mesh refinement study has been conducted. Together with theoretical considerations on the concentration boundary layer thickness as a function of the Pèclet number, it could be shown that about $35 \cdot \sqrt{\mathrm{Pe}}$ grid points in each direction have to be used for a grid-independent solution.

To validate the semi-Lagrangian advection scheme, different tests were conducted. One test was to compare the experimentally and theoretically predicted mass-transfer rates in Newtonian fluids. For this, the Sherwood number is plotted against the Reynolds-number in Figure 2. It can be seen that the results match other data in the range of their applicability very well. As expected the results do not follow the correlations for the flow around a solid cylinder. This is in agreement with simulations done by Khinast,[78] using a different simulation technique.

To validate the simulated flow field for the power-law fluid model, the computed drag coefficients were compared with correlations taken from the literature. This is illustrated in Figure 3. As can be seen, the agreement is good over the full range of computed Re-numbers.

It was already shown by us[78] that 2-D simulations can yield good results for mass transfer and chemical reactions in the vicinity of the bubble, since mass transfer is mainly influenced by the steep concentration gradient close to the interface. Only to a lesser extent it depends on the three-dimensional structure of the vortices of the downstream region of the flow. However, mixing effects induced by these vortices may differ significantly in the 2-D and 3-D case.

Mass-transfer coefficients as a function of the flow index

The dependence of the Sherwood number was studied as a function of the power law index n. As shown by Bhavaraju et al.,[79] the mass-transfer coefficient increases with increas-

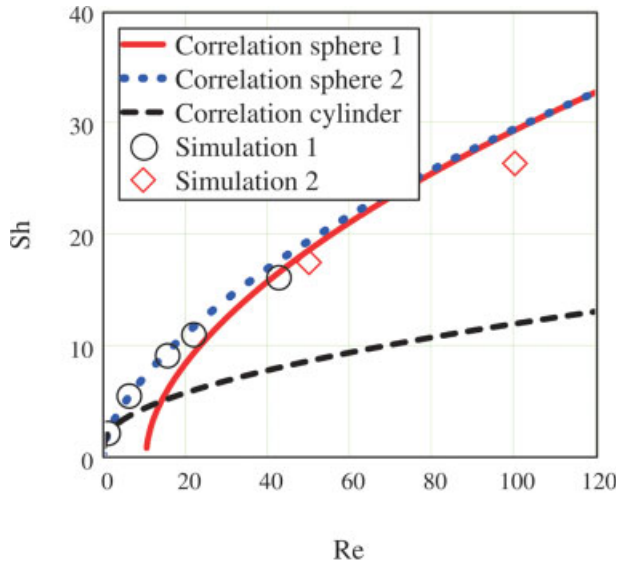

Figure 2. Sherwood number as a function of the Re-number for Newtonian fluids (Sc = 10).

Lines show correlations based on experimental data for solid cylinders (dashed line: low Re-number approximation) and spheres with mobile interfaces (solid line: high Re-approximation; dotted line: low to medium Re-number approximation); the symbols represent simulation results (diamonds: Khinast[78]; circles: this work). [Color figure can be viewed in the online issue, which is available at www.interscience.wiley.com.]

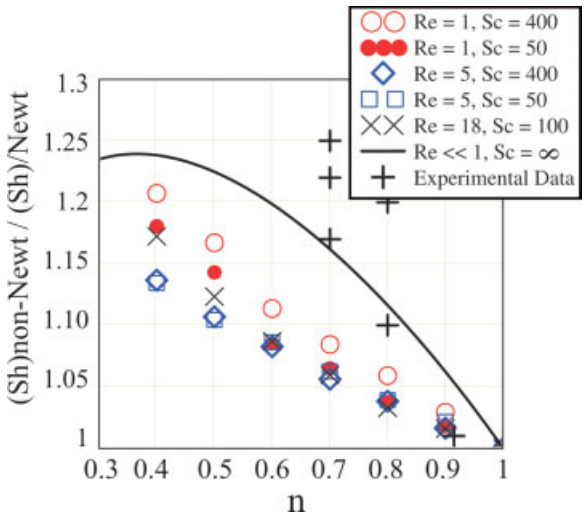

Figure 4. Sherwood number for power-law fluids divided by the Sherwood number for Newtonian fluids as a function of the flow index.

Circles, diamonds, boxes and crosses: simulation results; line: analytical expression by Hirose and Moo-Young,[80] +: experimental results for creeping flow by Moo-Young et al.[81] [Color figure can be viewed in the online issue, which is available at www.interscience.wiley.com.]

ing pseudo-plasticity and decreasing flow index. This trend can be confirmed in our simulations, as shown in Figure 4. The figure shows that the Sherwood number significantly

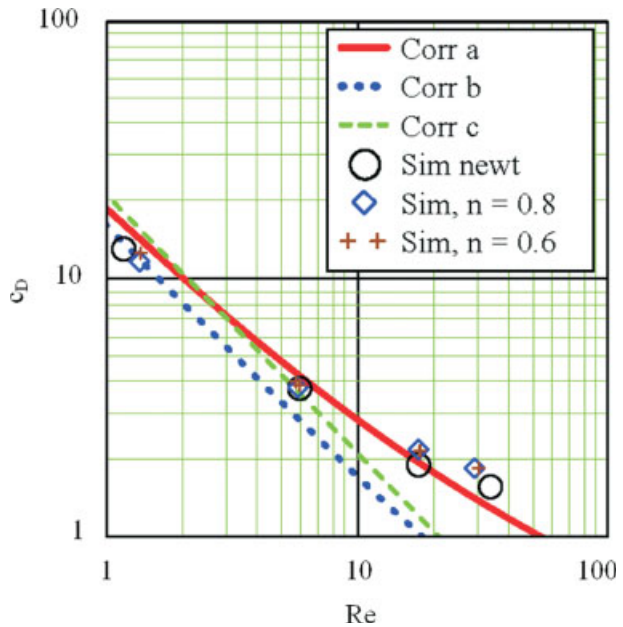

Figure 3. Drag coefficient as a function of the Re-number.

Corr a: Margaritis et al.[86]; Corr b: Rodrigue[87]; Corr c: Rodrigue et al.[68]; Sim newt: simulation results Newtonian fluid, Sim *n*: simulation results for power-law fluid with flow index *n*. [Color figure can be viewed in the online issue, which is available at www.interscience.wiley.com.]

increases with a decreasing shear index at constant Reynolds number, defined as $Re_{power\text{-}law} = d_b^n U_t^{(2-n)} \rho_l / K$. As can be seen from our simulations, the increase in the mass-transfer rate is more pronounced in the low-Reynolds-number regime Re = 1, compared to the case of Re = 5. However, also in the case of a recirculation wake (Re = 18) and at low flow indices, a significant enhancement of the mass-transfer coefficient can be observed. For such cases, shear thinning effects can cause an increase of the mass-transfer rate of up to 20%. Low values of the Schmidt number (Sc = 50) weaken the influence of shear thinning effects on the mass transfer at Re = 1, as in this flow, diffusion dominates convective effects. In the case of higher Schmidt numbers (Sc = 400), the concentration boundary layer is thinner and therefore develops in a region close to the bubble interface, where shear thinning effects lower the local viscosity. Thus, shear-thinning effects are more pronounced for higher Schmidt numbers.

In Figure 4 we have also included an analytical correlation derived by Hirose and Moo-Young,[80] which is valid in the limit of infinite Pèclet numbers and creeping flow. Furthermore, experimental data for creeping flow by Moo-Young et al.[81] are shown. As can be seen from Figure 4, our data for developed flows and realistic Sc number agree well with the trend of their theoretical and experimental analysis. As expected, the agreement improves for lower Reynolds number and higher the Schmidt numbers.

Inspection of the concentration field around a single bubble at Re = 5 shows, that bubbles in non-Newtonian liquids have a longer "tail" than those in Newtonian fluids (Figure 5). However, close to the bubble no qualitative differences between Newtonian and shear-thinning fluids can be seen in the region of low to moderate Re-numbers. Thus, only the reduced local viscosity close to the bubble interface and the

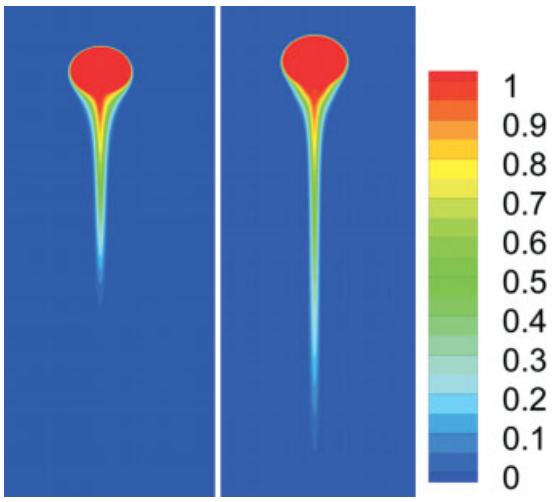

Figure 5. Concentration field around a bubble in Newtonian (left) and non-Newtonian liquids (right) (Re = 5, Sc = 400, n = 0.4).

[Color figure can be viewed in the online issue, which is available at www.interscience.wiley.com.]

higher viscosity in the wake of the bubble in non-Newtonian liquids must be responsible for the mass-transfer enhancement.

In order to illustrate these effects, the variation of the relative shear rate $\dot{\gamma}'$ in the vicinity of the bubble for Newtonian and non-Newtonian liquids was investigated. For that purpose the shear rate was normalized by a reference shear rate $\dot{\gamma}_{ref} = U_t/d_b$. In the vicinity of the bubble interface a higher peak value of the relative shear rate is observed for the shear-thinning fluid ($\dot{\gamma}'_{max} = 4.34$) compared to a Newtonian liquid ($\dot{\gamma}'_{max} = 3.56$). This higher peak value of the shear stress may have an effect on (biological) cells that are aggregated at the bubble interface.

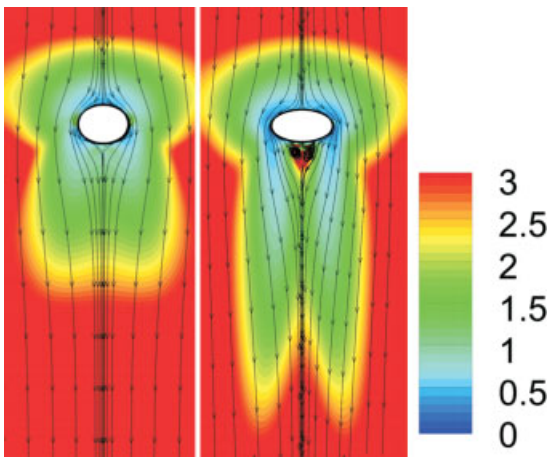

Figure 6. Relative viscosity ($\mu_{rel} = \mu/\mu_{Newt}$) field around a bubble rising in non-Newtonian liquids (left: Re = 5; right: Re = 18, n = 0.4).

[Color figure can be viewed in the online issue, which is available at www.interscience.wiley.com.]

The resulting viscosity field is shown in Figure 6. It clearly indicates that there exists a region in front of the bubble and two separated ones at the rear, where the viscosity is low. Because of the locally higher Re-number in those areas, the local mass transfer at the bubble roof will be higher than in Newtonian liquids. This explains the higher overall mass-transfer coefficient that was observed in non-Newtonian liquids at the same Reynolds number. Another finding is that at higher Re numbers, where a closed recirculating wake is formed, a confined region with high viscosity exists behind the bubble that influences the mass transfer from the bubble (Figure 6, right). This effect was first observed by Ohta et al.[82] who investigated bubble flow in a shear-thinning fluid via a Carreau-Yasuda model. The region becomes longer in the wake shedding regime and separates the two wake regions behind the bubble (Figure 7, upper left), which has an effect on the concentration distribution in the wake (Figure 7). Thus, when comparing the concentration fields for the different flow indices, a change in the mixing pattern can be observed. The lower the flow index, the lower the interaction between the left and right flow structure, which is due to the formation of a high viscosity zone which dampens the fluid motion and hinders mixing. Therefore, we conclude that mixing in the wake is negatively effected by the shear thinning effect, which may further reduce oxygen distribution in aerated low-shear-rate bioreactors.

Bubble swarms in non-Newtonian fluids

The dynamics of bubble swarms are highly complex due to the intricate and chaotic interactions between the bubbles. For example, most bubbles coalesce via a trailing bubble "bumping" into a leading one, i.e., there is an alignment of the trailing bubble, followed by acceleration and elongation.[83] Upon impact, a flattening of the contacting bubble

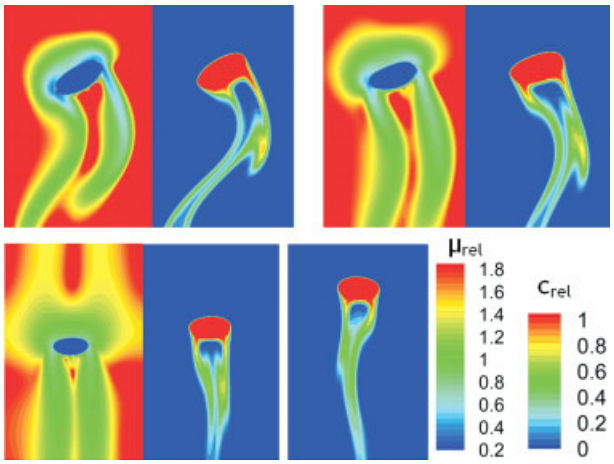

Figure 7. Relative viscosity ($\mu_{rel} = \mu/\mu_{Newt}$) and concentration ($c_{rel} = c/c_0$) profile in the wake of bubbles in non-Newtonian (upper left: n = 0.4; upper right: n = 0.6; lower left: n = 0.8) and Newtonian liquids (lower right) (Re = 28).

[Color figure can be viewed in the online issue, which is available at www.interscience.wiley.com.]

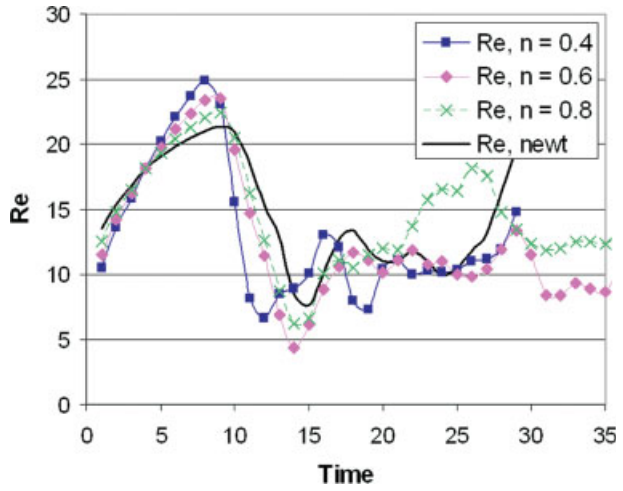

Figure 8. Re-number as a function of dimensionless time for a bubble swarm (Re_{av} = 12).

[Color figure can be viewed in the online issue, which is available at www.interscience.wiley.com.]

surfaces occurs, leaving a thin liquid film, which is typically 1–10 μm in thickness. The film drains until it is ~100 Å thick. Coalescence only occurs if the two bubbles are in contact longer than required for film drainage. Once the critical thickness is reached, an instability mechanism causes instantaneous film rupture and coalescence. The entire process occurs on a millisecond time-scale, the rate-determining step being film drainage.[84] Such processes become even more significant in non-Newtonian liquids, because bubbles trailing other bubbles will be exposed to a lower local viscosity in the leading bubble's wake. This leads to higher impact velocities and, in turn, to different coalescence characteristics. In order to study this problem, we recorded the mean velocity of the bubble swarm and the resulting Re-number, where as characteristic length the bubble's equivalent diameter was used.

To investigate this trend, in Figure 8 the instantaneous, swarm-averaged Re-number has been plotted as a function of dimensionless time for different flow indices. The time scale has been made dimensionless by a reference time $t_{ref} = d_b/U_t$, where U_t is the terminal rise velocity of a single bubble.

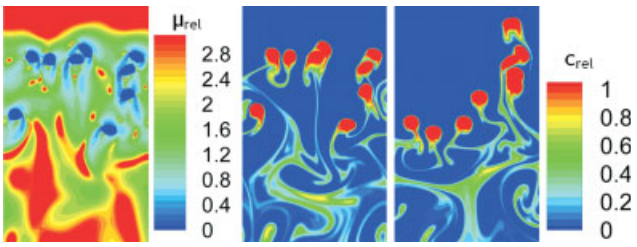

Figure 9. Relative viscosity ($\mu_{rel} = \mu/\mu_{Newt}$, left) and concentration field ($c_{rel} = c/c_0$, middle) around a bubble swarm (Re = 12, n = 0.6, t = 30).

The right picture shows the concentration field in a Newtonian liquid. [Color figure can be viewed in the online issue, which is available at www.interscience.wiley.com.]

The bubble swarms consists of nine bubbles, which would have a single-bubble Reynolds number of 20. A snapshot of the viscosity and concentration field in comparison to the Newtonian case is given in Figure 9. For these numerical experiments, the Eötvös number was chosen to be 2.81 and the viscosity (in the case of a Newtonian liquid) or the consistency index of the power-law model (in the case of a non-Newtonian liquid) was varied to give the specified single-bubble Reynolds number of 20. Thus, all single bubbles in the swarm would have the same single-bubble Re-number independent of the flow index. The starting conditions consisted of nine bubbles aligned in a 3 × 3 rectangular grid with a spacing of 1.5 bubble diameters between the bubble centers. The size of the computational domain was 6 × 18 bubble diameters in the horizontal and vertical position, respectively. From Figure 8 it can be seen that our expectation of the shear thinning effect can be confirmed. Although the time-averaged swarm Re-number remains essentially constant, bubble interactions are significantly enhanced, which is indicated by the higher amplitudes and higher frequency of the Re-number oscillations. Furthermore, by inspection we find that the bubbles in non-Newtonian liquids have higher approach velocities. This has no significant effect on mass transfer, but may impact coalescence of bubbles in a fundamental way. Further investigations will be needed to study this phenomenon.

As shown by Koynov et al.[30] the initial setup of the bubbles in the swarm and the number of bubbles has a significant impact on the swarm hydrodynamics. In order to study this effect, many different situations were probed. For example, a group of three bubbles was positioned in a horizontal line. While in the case of a Newtonian liquid the mean rise velocity is somewhat constant, we find a change in the flow regime when the power law index is decreased. This is illustrated in Figure 10, where the left bubble travels faster than the middle bubble and moves towards the center (Figure 10, left). As a consequence of the reduced local viscosity the left and center bubble begin to interact (Figure 10, right) and travel as mini-bubble cluster faster than the single bubble on the very right. This observation once more supports the conclusion that the aggregation of bubbles in non-Newtonian

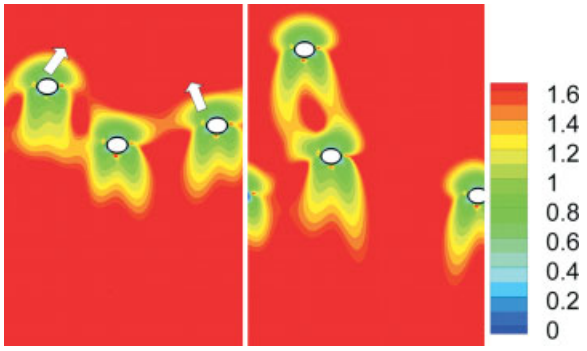

Figure 10. Relative viscosity ($\mu_{rel} = \mu/\mu_{Newt}$) field around three initially horizontally aligned bubbles (Re = 5).

[Color figure can be viewed in the online issue, which is available at www.interscience.wiley.com.]

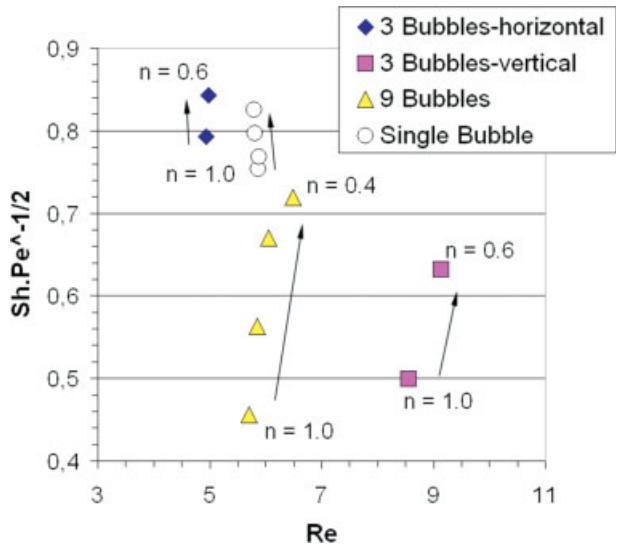

Figure 11. Mass-transfer coefficients from bubbles in swarms (arrows indicate decreasing flow index/increasing pseudoplasticity; Sc = 50).

[Color figure can be viewed in the online issue, which is available at www.interscience.wiley.com.]

liquids is enhanced. Thus, a change of bubble size due to coalescence in shear thinning liquids is more likely in comparison to Newtonian liquids.

Impact on mass transfer and mass-transfer enhancement by bubble clustering in non-Newtonian fluids is illustrated in Figure 11, where the enhancement factor is shown for bubble swarms with nine and three bubbles (two configurations) and for different flow indices. For the nine-bubble cluster (same setup as used for the investigation of the swarm Re-number) we find that the influence of the flow index on the mass-transfer coefficient is pronounced (Figure 11), with an increase of mass transfer up to 60%. Also in the case of three vertical bubbles a similar effect can be observed, which again is due to the strong hydrodynamic coupling that bubbles experience when traveling in the low-viscosity wake of others experience. For the nine-bubble cluster this effect is stronger than for the three vertically aligned bubbles (+49% vs. +28% for $n = 0.6$), due to the stronger bubble-bubble interactions. Also for the three horizontally aligned bubbles we find an increase in the mass-transfer rate, but this is quite moderate (+6% for $n = 0.6$).

Mass transfer in viscoelastic fluids

For the viscoelastic simulations, additional parameters such as time-step size, stress diffusivity for the stress smoothing, and the grid resolution were optimized to run a stable simulation. In our simulations we found that a higher gas-phase viscosity was needed to stabilize the simulation by smoothing the velocity field. A bubble viscosity of about 13% of the zero-shear-rate viscosity gave satisfactory stability.

A series of simulations for an aqueous 0.8 wt % Praestol 2500 polymer solution [Pilz C, Brenn G. Oral and written communication (data on the polymer solution), August 2006] has been performed based on variable relaxation times of the UCM model leading to different Deborah numbers. The other simulation parameters are listed in Table 1 and are based on the same dimensionless numbers as the experiments of Pilz and Brenn [Oral and written communication (data on the polymer solution), August 2006]. The Morton number was based on the zero shear viscosity μ_0. The infinite shear rate viscosity was related to μ_0 to obtain the relative infinite shear rate viscosity $\mu'_\infty = \mu_\infty/\mu_0$, which was used as simulation input. Evolution of the effective shear rate was described by the model used by Frank and Li[64] and Kemiha et al.[65] (refer to Eqs. 18 and 19).

Table 1. Input Parameters for the Simulation of Viscoelastic Fluids – UCM Model

Shear Thinning Model	Carreau Model
Relative infinite shear rate viscosity, μ'_∞	0.0109
Parameter a (Carreau model)	1.35
Parameter n (Carreau model)	0.333
Parameter for the evolution of the viscosity, t_{r0}	12.0
Parameter for the evolution of the viscosity, ϕ_0	0.50
Deborah number, De	0–8
Stress diffusivity, κ	0.01
Grid resolution	140 × 420
Domain size	$6d_b \times 18d_b$
Time step size, Δt	0.001
Morton number, Mo	234
Eötvös number, Eö	2.81

In Figure 12 the normalized τ_{yy} stress distribution and the streamlines of the resulting flow fields are shown. While in the case of an inelastic fluid (De = 0) a clear fore-aft symmetry of the streamlines is observed, in viscoelastic fluids this is not the case, and the occurrence of a negative wake is observed. Furthermore, high τ_{yy} stresses are found in the rear region of the bubble. This stress is responsible for bubble deformation. However, in the current simulations the bubble

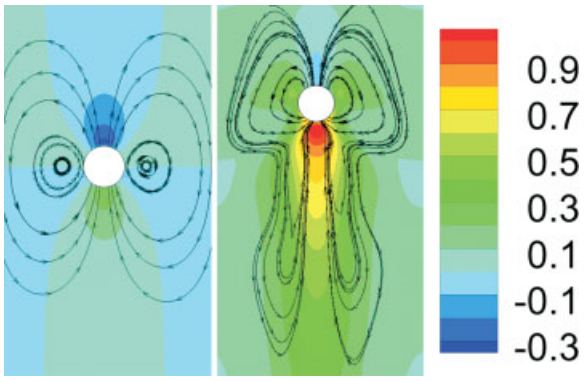

Figure 12. Relative normal stress ($\tau_{yy,rel} = \tau_{yy}/\tau_{yy,max}$) distribution surrounding bubbles in non-Newtonian fluids (UCM model; left: inelastic fluid, De = 0, Re = 0.029; right: viscoelastic fluid, De = 5.58, Re = 0.319).

[Color figure can be viewed in the online issue, which is available at www.interscience.wiley.com.]

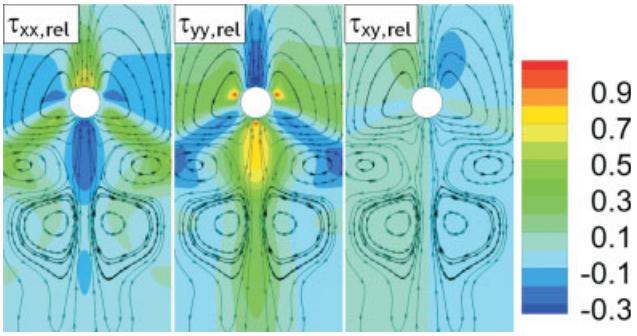

Figure 13. Relative stress ($\tau_{rel} = \tau/\tau_{yy,max}$) distribution surrounding bubbles in non-Newtonian fluids (Giesekus model, De = 3.84, Re = 0.317).

[Color figure can be viewed in the online issue, which is available at www.interscience.wiley.com.]

shape could not be predicted accurately, due to the UCM constitutive equation, which cannot predict a realistic extensional viscosity which is responsible for bubble deformation. Furthermore, a fully developed negative wake was not observed in the simulations, as seen in experimental studies.[65] Therefore, we conducted simulations based on the Giesekus and Phan-Thien model, which yielded better results with respect to the negative wake formation, as can be seen in Figure 13 for the Giesekus model. However, for the mass-transfer simulations we used the UCM model, since only one parameter (the relaxation time) is necessary to characterize the elasticity of the liquid phase.

In Figure 14 the evolution of the rise velocity is shown as a function of the vertical bubble position. The bubble position has been made dimensionless with the bubble diameter. Clearly, even in the case of a small Deborah number (De = 0.52) the steady-state bubble rise velocity is significantly higher than in the case of an inelastic fluid (De = 0) and velocity oscillations upon start-up are observed. For example, in the test case we find a Re-number of 0.029 in the case of no elasticity and a Re-number of 0.319 in the case of De = 5.6. This is due to the ability of viscoelastic fluids to absorb deformation in an elastic way. Thus, when the relaxation time in the UCM model is increased, some of the potential energy of the bubble is not dissipated but used for the acceleration of the bubble and the surrounding liquid. This leads to a higher rise velocity, which in turn enhances the mass transfer from the bubble's interface due to the increased convective flow and better mixing. Furthermore, the bubble deforms and becomes elongated.

The existence of a negative wake behind bubbles in viscoelastic fluids is expected to improve dispersion of the dissolved gas phase. Our simulations of the concentration fields in the wake of viscoelastic fluids confirm our expectation. This is illustrated in Figure 15 (lower right figure), where the downward motion of the negative wake leads to a convective transport of dissolved gas into the liquid bulk phase, away from the bubble trajectory. We also observe an increased mass transfer, as shown in Figure 16, which shows the Sh $Pe^{-0.5}$ number as a function of the position of the bubble for different Deborah numbers. It can be seen that in all cases with elastic features an increased mass-transfer rate is observed. However, the values do not change significantly above a Deborah number of O(1). Therefore, we assume that

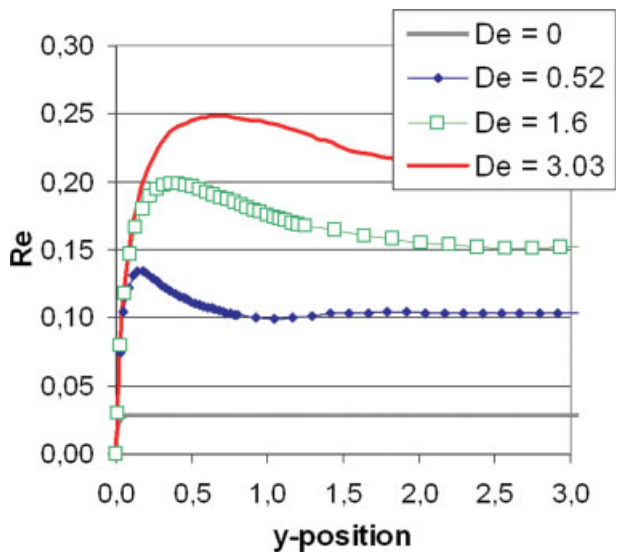

Figure 14. Reynolds number as a function of vertical bubble position for different Deborah numbers (UCM model, simulation parameters according to Table 1).

[Color figure can be viewed in the online issue, which is available at www.interscience.wiley.com.]

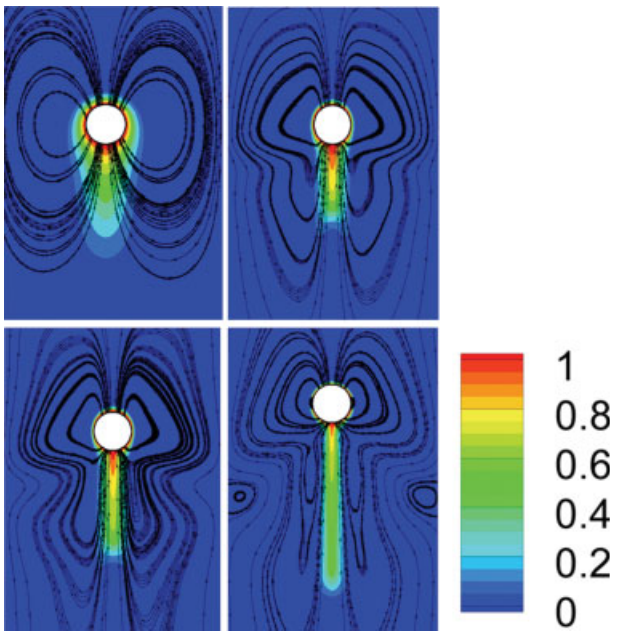

Figure 15. Streamlines and concentration fields surrounding bubbles in viscoelastic fluids (upper left: De = 0; upper right: De = 1.6; lower left: De = 3.0; lower right: De = 5.6; Sc = 1000).

[Color figure can be viewed in the online issue, which is available at www.interscience.wiley.com.]

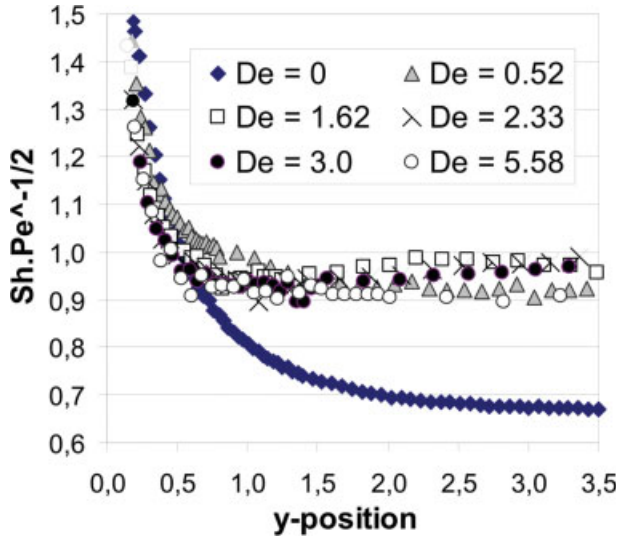

Figure 16. Sherwood numbers of bubbles in viscoelastic fluids at different Deborah numbers (Sc = 1000).

[Color figure can be viewed in the online issue, which is available at www.interscience.wiley.com.]

the increased mass transfer is mainly due to convective effects, which is supported by the fact that Sh $Pe^{-0.5}$ remains approximately constant.

Summary and Conclusion

In our work it was shown that simulations of bubbly flows with mass transport in non-Newtonian media at the microscale are feasible. The rheology of shear-thinning fluids can be implemented in a straightforward way. However, inclusion of the fluid's elasticity remains a challenging task that has been addressed successfully for UCM, Giesekus and Phan-Thien models. Even concentration fields and mass-transfer coefficients could be predicted. While current simulations are restricted to moderate Re-numbers and realistic Sc-numbers, future developments will allow a precise characterization of realistic systems at high Reynolds and Schmidt numbers or/and for 3-D cases.

For the motion of bubbles in purely viscous fluids we draw the following conclusions:

- The qualitative flow structure in shear-thinning fluids remains basically the same as in Newtonian fluids. Behind the bubble a region with high viscosity is observed, leading to the formation of two separated zones in the vortex-shedding regime that have influence on the dissolved gas dispersion in the wake.
- Due to the shear thinning effect, mass transfer around a single bubble is increased with decreasing flow index (increasing pseudoplasticity).
- In bubble swarms, the flow index has a significant impact on the fluid dynamics and on mass-transfer rates due to the different interactions of bubbles in the local variable viscosity field.

The results from the simulation of bubble flows in viscoelastic fluids can be summarized as follows:

- The simulation of viscoelastic fluids is only possible if special numerical methods are applied. In addition, more stringent requirements on grid resolution and time stepping have to be imposed, since no general stability criteria exist.
- The fluid dynamics and the mass-transfer characteristics change significantly in the presence of fluid elasticity. Therefore, the elastic features of a fluid need to be accounted for. It is not sufficient to characterize such media with simple non-Newtonian fluid models.
- In our simulations with the UCM model, the formation of a negative wake was observed. However, a fully developed negative wake was not found even in simulations involving a Giesekus and Phan-Thien model.
- Mass transfer in the case of fluid elasticity is significantly higher compared to cases where only shear-thinning effects are considered. This mass-transfer enhancement is mainly due to the increased Re-number. We therefore draw the conclusion that the complex wake structure in the bubble flow of viscoelastic fluids has only a limited effect on the mass-transfer rate. However, it has a strong impact on the dispersion of dissolved gas.

Acknowledgments

The authors thank Prof. Guenter Brenn and Christian Pilz (Department of Fluid Dynamics and Heat Transfer, Graz University of Technology) for many helpful discussions and for providing experimental data on bubbles in viscoelastic fluids. JGK acknowledges partial funding of this work through NSF Grant CTS 02098764 and the EU Marie Curie Chair MEXC-CT-2004-006767.

Notation

a = parameter of the Carreau-Yasuda model
a = specific gas–liquid interphase (m^2/m^3)
c_α = concentration of species α (kmol/m^3)
c_D = drag coefficient
CFD = computational Fluid Dynamics
D = rate of strain tensor (1/s)
De = deborah number ($De = t_m \cdot U_l/d_b$)
$D\alpha$ = diffusion coefficient of species α (m^2/s)
d_b = volume equivalent bubble diameter (m)
DNS = direct Numerical Simulation
ds' = differential element of the bubble contour (m)
ECL-AL = external Circulating Loop Airlift Bioreactors
Eo = Eötvös number ($Eo = g \cdot \Delta\rho \cdot {d_b}^2/\sigma$)
$\vec{f}$ = body force (gravity; m/s^2)
$\vec{F}_\sigma$ = body forces and surface tension (N/m^3)
G = relaxation Function (Pa)
h = reference length (m)
k = reaction rate constant [m^3/(kmol s)]
K = consistency index of the power law model ($Pa \cdot s^n$)
K = right-hand side of UCM model
K_{Spring} = elasticity of the Hookean Spring (Pa)
l_κ = stress diffusive length (m)
$l\mu$ = viscous length scale (m)
Mo = morton number ($Mo = g \cdot {\mu_l}^4 \cdot \Delta\rho/{\rho_l}^2 \cdot \sigma^3$)
N = time step (used as superscript)
N = flow index of the power law model
$\vec{n}'$ = normal vector to the bubble interface
n_{CY} = parameter of the Carreau-Yasuda model
p = pressure (Pa)
r_j = reaction rate of the jth reaction [kmol/($m^3 \cdot s$)]
PDE = partial differential equation
Pe = Péclet number ($Pe = d_b \cdot U_t \cdot \rho_l/D_\alpha$)

Re = Bubble Reynolds number ($\mathrm{Re}_{\mathrm{newt}} = d_b \cdot U_t \cdot \rho_l/\mu_l$, $\mathrm{Re}_{\mathrm{power\text{-}law}} = d_b^n \cdot U_t^{(2-n)} \cdot \rho_l/K$)
Sh = Sherwood number ($\mathrm{Sh} = \beta \cdot d_b/D\alpha$)
Sc = Schmidt number ($\mathrm{Sc} = \mu_l/\rho_l \cdot D\alpha$)
s = time parameter in the relaxation function (s)
t = time (s)
t_m = relaxation time (s)
$t_{r,0}$ = parameter for the evolution of the viscosity (s)
$\vec{u}$ = velocity vector (m/s)
$\vec{u}^*$ = intermediate velocity vector (m/s)
U_t = terminal rise velocity (m/s)
Wi = weissenberg number ($\mathrm{Wi} = t_m \cdot \dot{\gamma}$)
$\vec{x}$ = orthogonal coordinates, position vector of a point
$\vec{x}'$ = orthogonal coordinate of the interface

Greek letters

α = Courant number
β = mass-transfer coefficient (m/s)
β = minimum relative wavelength
δ = Dirac delta function
φ = effective shear rate (1/s)
φ_0 = parameter for the evolution of the viscosity (1/s)
$\dot{\gamma}$ = shear rate (1/s)
$\dot{\gamma}'$ = dimensionless shear rate
η = fluid dynamic length scale (m)
η_B = Batchelor length scale (m)
κ' = curvature
κ = artificial stress diffusivity
λ = parameter of the Carreau-Yasuda model (s)
μ = dynamic viscosity (Pa · s)
μ' = dimensionless dynamic viscosity
μ_∞ = infinite shear rate viscosity of the Carreau-Yasuda model (Pa · s)
μ'_∞ = relative infinite shear rate viscosity of the Carreau-Yasuda model
μ_0 = zero shear rate viscosity of the Carreau-Yasuda model (Pa · s)
$\nu_{\alpha,j}$ = stoichiometric coefficient of species α in reaction j
ρ = density (kg/m^3)
σ = surface tension (N/m)
τ = stress tensor (Pa)

Literature Cited

1. Leduy A, Marsan AA, Coupal B. A study of the rheological properties of a non-Newtonian Fermentation broth. *Biotechnol Bioeng*. 1974;16:61–76.
2. Curtis W, Emery A. Plant cell suspension culture rheology. *Biotechnol Bioeng*. 1993;42:520–526.
3. Kieran PM, McLoughlin P, Malone D. Plant Cell suspension cultures: some engineering considerations. *J Biotechnol*. 1997;59:39–52.
4. Doran P. Design of mixing systems for plant cell suspensions in stirred reactors. *Biotechnol Prog*. 1999;16:319–335.
5. Rodriguez-Monroy M, Galindo E. Broth rheology, growth and metabolite production of *Beta vulgaris* suspension culture: a comparative study between cultures grown in shake flasks and in a stirred tank. *Enzyme Microb Technol*. 1999;24:687–693.
6. Rodriguez-Monroy M, Galindo E. Production of arabinogalactan proteins in *Beta vulgaris* cell suspension cultures: a response to hydrodynamic stress. In: Notthnagel E, Basic A, Clarke A, editors. Cell and Developmental Biology of Arabinogalactan-Proteins. New York: Kluwer Academic, 2000:290–292.
7. Badino AC Jr, Facciotti MCR, Schmidell W. Volumetric oxygen transfer coefficients (k_La) in batch cultivations involving non-Newtonian broths. *Biochem Eng J*. 2001;8:111–119.
8. Sánchez MJ, Jiménez-Aparicio A, López GG, Tapia GT, Rodríguez-Monroy M. Broth rheology of *Beta vulgaris* cultures growing in an air lift bioreactor. *Biochem Eng J*. 2002;12:37–41.
9. Kawase Y, Hashimoto N. Gas hold-up and oxygen transfer in three-phase external-loop airlift bioreactors: non-Newtonian fermentation broths. *J Chem Tech Biotechnol*. 1996;65:325–334.
10. Li GQ, Qui HW, Zheng ZM, Cai ZL, Yang SZ. Effect of fluid rheological properties on mass transfer in a bioreactor. *J Chem Tech Biotechnol*. 2004;65:385–391.
11. Jin B, Lant P, Ge X. Hydrodynamics and mass transfer coefficient in activated sludge aerated stirred column reactor: experimental analysis and modeling. *Biotechnol Bioeng*. 2005;91:406–417.
12. Al-Masry WA. Effect of scale-up on average shear rates for aerated non-Newtonian liquids in external loop airlift reactors. *Biotechnol Bioeng*. 1999;62:494–498 (Communication to the editor).
13. Choi JH, Keum KC, Lee SY. Production of recombinant proteins by high cell density culture of *Escherichia coli*. *Chem Eng Sci*. 2006; 61:876–885.
14. Duddridge JE, Kent CA, Laws JF. Effect of surface shear stress on the attachment of *Pseudomonas fluorescens* to stainless steel under defined flow conditions. *Biotechnol Bioeng*. 1982;24:153–164.
15. Kieran PM. *An Investigation of the Hydrodynamic Shear Susceptibility of Suspension Cultures of Morinda citrifolia*. PhD Thesis. Dublin, Ireland: University College, 1993.
16. Lau YL, Liu D. Effect of flow rate on biofilm accumulation in open channels. *Water Res*. 1993;27:355–360.
17. Gjaltema A, Tijhuis L, van Loosdrecht MCM, Heijnen JJ. Detachment of biomass from suspended nongrowing spherical biofilms in airlift reactors. *Biotechnol Bioeng*. 1995;46:258–269.
18. Gjaltema A, van der Marel N, Loosdrecht MCM, Heijnen JJ. Adhesion and biofilm development on suspended carriers in airlift reactors: hydrodynamic conditions versus surface characteristics. *Biotechnol Bioeng*. 1997;55:880–889.
19. Leenen EJTM, Martins dos Santos VAP, Grolle KCF, Tramper J, Wijffels RH. Characteristics of and selection criteria for cell immobilisation in wastewater treatment. *Water Res*. 1996;30:2895–2996.
20. Martins dos Santos VAP, Leenen EJTM, Rippoll MM, van der Sluis C, Vliet T, Tramper J, Wijffels RH. Relevance of rheological properties of gel beads for their mechanical stability in bioreactors. *Biotechnol Bioeng*. 1997;56:517–529.
21. Ma N, Koelling KW, Chalmers JJ. Fabrication and use of a transient contractional flow device to quantify the sensitivity of mammalian and insect cells to hydrodynamic forces. *Biotechnol Bioeng*. 2002; 80:428–437.
22. Mollet M, Ma N, Zhao Y, Brodkey R, Taticek R, Chalmers JJ. Bioprocess equipment: characterization of energy dissipation rate and its potential to damage cells. *Biotechnol Prog*. 2004;20:1437–1448.
23. Nienow AW. Reactor engineering in large scale animal cell culture. *Cytotechnology*. 2006;50:9–33.
24. Meier ST, Hatton TA, Wang DIC. Cell death from bursting bubbles: role of cell attachment to rising bubbles in sparged reactors. *Biotechnol Bioeng*. 1999;62:468–478.
25. Ma N, Chalmers JJ, Aunins JG, Zhou W, Xie L. Quantitative studies of cell-bubble interactions and cell damage at different pluronic F-68 and cell concentrations. *Biotechnol Prog*. 2004;20:1183–1191.
26. Koynov A, Khinast J. Micromixing in reactive, deformable bubble, and droplet swarms. *Chem Eng Technol*. 2006;29:13–23.
27. Koynov A, Tryggvason, Khinast J. Characterization of the localized hydrodynamic shear forces and dissolved oxygen distribution in sparged bioreactors. *Biotechnol Bioeng*. 2007;97:317–331.
28. Richard A, Margaritis A. Rheology, oxygen transfer, and molecular weight characteristics of poly(glutamic acid) fermentation by *Bacillus subtilis*. *Biotechnol Bioeng*. 2003;82:299–305.
29. Tryggvason G, Bunner B, Esmaeeli A, Juric D, Al-Rawahi N, Tauber W, Han J, Nas S, Jan Y-J. A front-tracking method for the computations of multiphase flow. *J Comput Phys*. 2001;169:708–759.
30. Koynov A, Khinast J, Tryggvason G. Mass transfer and chemical reactions in bubble swarms with dynamic interfaces. *AIChE J*. 2005;51:2786–2800.
31. Bandyopadhyay B, Humphrey AE, Taguchi H. Dynamic measurement of the volumetric oxygen transfer coefficient in fermentation systems. *Biotechnol Bioeng*. 1967;9:533–544.
32. Benyahia F, Jones L. Scale effects on hydrodynamic and mass transfer characteristics of external loop airlift reactors. *Chem Tech Biotechnol*. 1997;69:301–308.
33. Kawase Y, Halard B, Moo-Young M. Liquid-phase mass transfer coefficients in bioreactors. *Biotechnol Bioeng*. 1992;39:1133–1140.

34. Deen NG, Solberg T, Hjertager BH. Flow generated by an aerated rushton impeller: two-phase PIV experiments and numerical simulations. *Can J Chem Eng*. 2002;80:1–15.
35. Matos EM, Nunhez JR. The effect of different feed flow patterns on the conversion of bubble column reactors. *Chem Eng J*. 2006;116: 163–172.
36. Melheim JA, Chiesa M. Simulation of turbulent electrocoalescence. *Chem Eng Sci*. 2006;61:4540–4549.
37. Vennerk BCH, Derksen JJ, Van der Akker HEA. Population balance modeling of aerated stirred vessels based on CFD. *AIChE J*. 2002; 48:673–685.
38. Derksen JJ. Numerical simulation of solids suspension in a stirred tank. *AIChE J*. 2003;49:2700–2714.
39. Darmana D, Deen NG, Kuipers JAM. Detailed modeling of hydrodynamics, mass transfer and chemical reactions in a bubble column using a discrete bubble model. *Chem Eng Sci*. 2005;60:3383–3404.
40. Darmana D. *On the Multiscale Modeling of Hydrodynamics, Mass Transfer and Chemical Reactions in Bubble Columns*. PhD Thesis. Twente, Netherlands: University of Twente, 2006.
41. Pera C, Réveillon J, Vervisch L, Domingo P. Modeling subgrid scale mixture fraction variance in LES of evaporating spray. *Combust Flame*. 2006;146:635–648.
42. Pitsch H. Large-eddy simulation of turbulent combustion. *Annu Rev Fluid Mech*. 2006;38:453–482.
43. Joshi JB. Computational flow modeling and design of bubble column reactors. *Chem Eng Sci*. 2001;56:5893–5933.
44. Deen NG, van Sint Annaland M, Kuipers JAM. Multi-scale modeling of dispersed gas-liquid two-phase flow. *Chem Eng Sci*. 2004;59: 1853–1861.
45. Akbar MK, Ghiaasiaan SM. Simulation of Taylor flow in capillaries based on the volume-of-fluid technique. *Ind Eng Chem Res*. 2006; 45:5396–5403.
46. Bothe D, Schmidtke M, Warnecke H-J. VOF-simulation of the lift force for single bubbles in a simple shear flow. *Chem Eng Technol*. 2006;29:1048–1053.
47. Shopov PJ, Minev PD. The unsteady motion of a bubble or drop towards a liquid liquid interface. *J Fluid Mech*. 1992;235:123–141.
48. Hu HH, Patankar NA, Zhu MY. Direct numerical simulations of fluid-solid systems using the arbitrary Lagrangian-Eulerian technique. *J Comput Phys*. 2001;169:427–462.
49. Ryskin GR, Leal LG. Numerical solution of free-boundary problems in fluid-mechanics, Part 1. The finite difference technique. *J Fluid Mech*. 1984;148:1–17.
50. Ryskin GR, Leal LG. Numerical solution of free-boundary problems in fluid-mechanics, Part 2. Buoyancy driven motion of a gas bubble through a quiescent liquid. *J Fluid Mech*. 1984;148:19–35.
51. Unverdi SO, Tryggvason G. A front-tracking method for viscous, incompressible multi-fluid flows. *J Comput Phys*. 1992;100:25–37.
52. Radl S, Khinast J. Prediction of mass transfer coefficients in non-Newtonian fermentation broths using first-principles methods. *Biotechnol Bioeng*. In press.
53. Townsend P. On the numerical simulation of two-dimensional time-dependent flows of Oldroy fluids, Part 1: basic method and preliminary result. *J Non-Newtonian Fluid Mech*. 1984;14:265–278.
54. Keunings R. On the high Weissenberg number problem. *J Non-Newtonian Fluid Mech*. 1986;20:209–226.
55. Crochet MJ, Davies AR, Walters K. Numerical Simulation of Non-Newtonian Flow. Amsterdam, Netherlands: Elsevier, 1984.
56. Marchal JM, Crochet MJ. A new mixed finite element for calculating viscoelastic flow. *J Non-Newtonian Fluid Mech*. 1987;26:77–114.
57. Gerritsma M. *Time Dependent Numerical Simulation of a Viscoelastic Fluid on a Staggered Grid*. PhD Thesis. Groningen, Netherlands: University of Groningen, 1996.
58. Sun J, Phan-Thien N, Tanner RI. An adaptive viscoelastic stress splitting scheme and its applications: AVSS/SI and AVSS/SUPG. *J Non-Newtonian Fluid Mech*. 1996;65:75–91.
59. Baaijens FPT. Mixed finite element methods for viscoelastic flow analysis: a review. *J Non-Newtonian Fluid Mech*. 1998;79:361–385.
60. Ellero M. *Smoothed Particle Dynamics Methods the Simulation of Viscoelastic Fluids*. PhD Thesis. Berlin, Germany: TU Berlin, 2004.
61. Fattal R, Kupferman R. Time-dependent simulation of viscoelastic flows at high Weissenberg number using the log-conformation representation. *J Non-Newtonian Fluid Mech*. 2005;126:23–37.
62. Hulsen MA, Fattal R, Kupferman R. Flow of viscoelastic fluids past a cylinder at thigh Weissenberg number: stabilized simulations using matrix logarithms. *J Non-Newtonian Fluid Mech*. 2005;127:27–39.
63. McKinley GH. Steady and transient motion of spherical particles in viscoelastic liquids. In: Chhabra R, De Kee D, editors. Transport Processes in Bubbles, Drops and Particles, 2nd ed. New York, NY: Taylor & Francis, 2002.
64. Frank X, Li HZ. Complex flow around a bubble rising in a non-Newtonian fluid. *Phys Rev E*. 2005;71:036309.
65. Kemiha M, Frank X, Poncin S, Li HZ. Origin of the negative wake behind a bubble rising in non-Newtonian fluids. *Chem Eng Sci*. 2006;61:4041–4047.
66. Astarita G, Aapuzzo G. Motion of gas bubbles in non-Newtonian liquids. *AIChE J*. 1965;11:815–820.
67. Hassager O. Negative wake behind bubbles in non-Newtonian liquids. *Nature*. 1979;279:402–403.
68. Rodrigue D, De Kee D, Chan Man Fong CF. Bubble velocities: further developments on the jump discontinuity. *J Non-Newtonian Fluid Mech*. 1998;79:45–55.
69. Rodrigue D, De Kee D. Bubble velocity jump discontinuity in polyacrylamide solutions: a photographic study. *Rheol Acta*. 1999;38: 177–182.
70. Herrera-Velarde JR, Zenit R, Chehata D, Mena B. The flow of non-Newtonian fluids around bubbles and its connection to the jump discontinuity. *J Non-Newtonian Fluid Mech*. 2003;111:199–209.
71. Böhme G. *Strömungsmechanik Nichtnewtonscher Fluide,* 2nd ed. Stuttgart, Germany: B.G. Teubner, 2000.
72. Sarkar K, Schowalter WR. Deformation of a two-dimensional viscoelastic drop at non-zero Reynolds number in time-periodic extensional flows. *J Non-Newtonian Fluid Mech*. 2000;95:315–342.
73. Gaskell PH, Lau AKC. Curvature-compensated convective transport: SMART, a new boundedness-preserving transport algorithm. *Int J Numer Methods Fluids*. 1988;8:617–641.
74. Sureshkumar R, Beris AN. Effect of artificial stress diffusivity on the stability of numerical calculations and the flow dynamics of time-dependent viscoelastic flows. *J Non-Newtonian Fluid Mech*. 1995;60:53–80.
75. Atalik K, Keunings R. Non-linear temporal stability analysis of viscoelastic plan channel flows using a fully-spectral method. *J Non-Newtonian Fluid Mech*. 2002;102:299–319.
76. Staniforth A, Côté J. Semi-Lagrangian integration schemes for atmospheric models—a review. *Mon Weather Rev*. 1991;119:2006–2223.
77. Spiegelman M, Katz RF. A semi-Lagrangian Crank-Nicholson algorithm for the numerical solution of advection-diffusion problems. Available at http://www.ldeo.columbia.edu/~mspieg/SLCN_paper.pdf (accessed May 02, 2006).
78. Khinast J. Impact of 2-D bubble dynamics on the selectivity of fast gas–liquid reactions. *AIChE J*. 2001;47:2304–2319.
79. Bhavaraju SM, Mashelkar RA, Blanch HW. Bubble motion and mass transfer in non-Newtonian fluids, part 1: single bubble in power law and Bingham fluids. *AIChE J*. 1978;24:1063–1070.
80. Hirose T, Moo-Young M. Bubble drag and mass transfer in non-Newtonian fluids: creeping flow with power-law fluids. *Can J Chem Eng*. 1969;47:265–267.
81. Moo-Young M, Hirose T, Ali S. Rheological effects on liquid phase mass transfer in two phase dispersions: results for creeping flow. In: *Proceedings of Fifth International Congress on Rheology*, Kyoto, 1970:233.
82. Ohta M, Iwasaki E, Obata E, Yoshida Y. Dynamic processes in a deformed drop rising through shear-thinning fluids. *J Non-Newtonian Fluid Mech*. 2005;132:100–107.
83. Bhaga D, Weber ME. In-line interaction of a pair of bubbles in a viscous liquid. *Chem Eng Sci*. 1980;35:2467–2474.
84. Tse K, Martin T, McFarlane CM, Nienow AW. Visualization of bubble coalescence in a coalescence cell, a stirred tank and a bubble column. *Chem Eng Sci*. 1998;53:4031–4036.
85. Balay S, Buschelman K, Eijkhout V, Gropp WD, Kaushik D, Knepley MG, McInnes LC, Smith BF, Zhang H. PETSc User Manual ANL-95/11, Revision 2.1.5. Illinois: Argonne National Laboratory, 2004.

86. Margaritis A, te Bokkel DW, Karamev DG. Bubble rise velocities and drag coefficients in non-Newtonian polysaccharide solutions. *Biotechnol Bioeng*. 1999;64:257–266.
87. Rodrigue D. A simple correlation for gas bubbles rising in power-law fluids. *Can J Chem Eng*. 2002;80:289–292.

Appendix A: Boundary and Initial Conditions

Especially in the case of a viscoelastic fluid, choice of consistent initial and boundary conditions is of central importance. While the initial conditions for velocity and pressure do not need any special consideration, consistent initial values for the stress terms are important for the convergence of the iterative scheme in steady-state simulations. Typically the stress field of Newtonian fluid is used as first guess. As our simulations are unsteady, we always start with a bubble at rest in a quiescent fluid. Thus, all velocities and stresses are zero initially.

In the case of periodic-box simulations, the complete strain history of the fluid (and the stress history) is known, as the inflow at the bottom of the domain equals the outflow at the top. Similarly, the left and right borders are connected. This was implemented by the use of ghost points at the domain boundary, which were updated within each iteration cycle.

For simulations including solid boundaries, the stresses at the boundary points (these points are not directly involved in the solution procedure) have to be defined (Fig. A1). For the velocity components the approach is straightforward. The no-slip boundary condition was implemented by setting

$$\left(u_{i,1} + u_{i,2}\right)/2 = u_{\text{wall}}. \tag{A1}$$

Thus, the first grid point outside the computational domain was set $u_{i,1} = 2 \cdot u_{\text{wall}} - u_{i,2}$. For the second-order velocity derivatives the ghost point is calculated as $u_{i,1} = \left(8 \cdot u_{\text{wall}} - 6 \cdot u_{i,2} + u_{i,3}\right)$. In the case of stresses the situation is more complicated. Gerritsma[57] reported that for viscoelastic flows a linear approximation of the velocity should be chosen due to stability concerns. Using such a linear velocity extrapolation, Deborah numbers in the order of O(10) should be attainable.

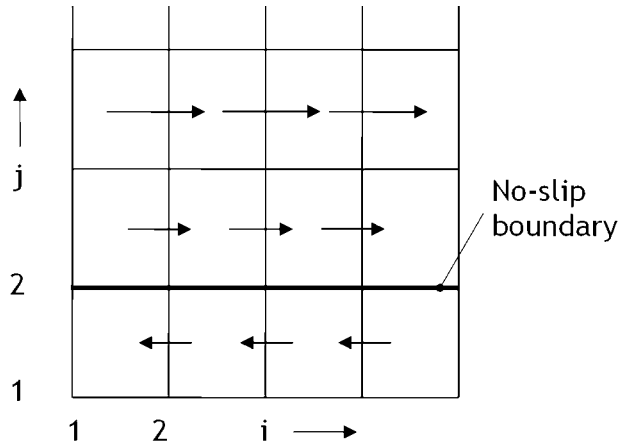

Figure A1. Definition of velocities outside the computational domain (zero-wall velocity).

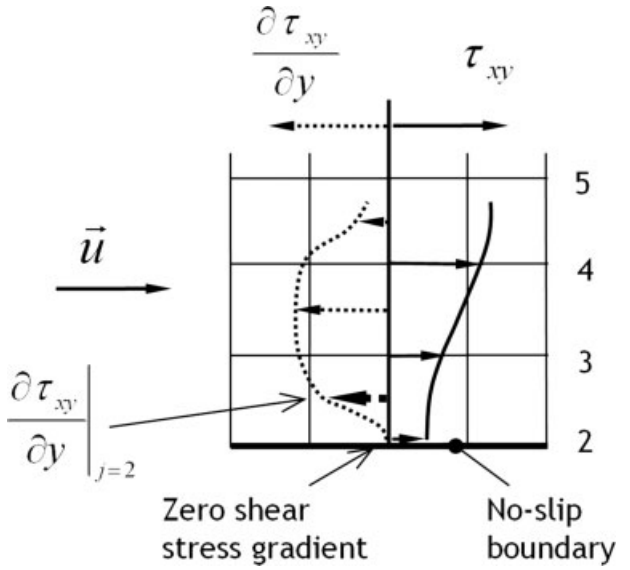

Figure A2. Definition of shear stress and shear-stress gradient at the wall.

At the wall the following relations hold (assuming a wall in x-direction)

$$u|_{j=1} = v|_{j=1} = \left.\frac{\partial u}{\partial x}\right|_{j=1} = \left.\frac{\partial v}{\partial y}\right|_{j=1} = 0. \tag{A2}$$

Thus, the velocity gradient tensor and the rate-of-strain tensor only have off-diagonal elements. This implies that all viscous normal stresses are equal to zero, and therefore, the source term on the right hand side of the UCM model vanishes at the wall. Thus, all normal stresses will go to zero with a time constant depending on the relaxation time. Furthermore, normal stresses at the wall that have been zero initially will remain zero.

In the UCM framework, only the stress τ_{yy} (stress normal to the wall) is needed for the calculation of the shear stress at the wall:[57]

$$\tau_{xy}|_{j=1} = \tau_{xy}|_{j=2} + \Delta t \cdot \left.\frac{\partial u}{\partial y}\right|_{j=1} \cdot \tau_{yy}|_{j=1}. \tag{A3}$$

Since normal stresses are equal zero at the wall

$$\tau_{xy}|_{j=1} = \tau_{xy}|_{j=2}. \tag{A4}$$

Thus, the shear stress gradient at the wall is zero, and we can interpolate the shear stress gradient at the last cell center, using the two adjacent grid cells in the domain (Fig. A2), i.e.,

$$\left.\frac{\partial \tau_{xy}}{\partial y}\right|_{j=nyp1} = \frac{2}{3} \cdot \left.\frac{\partial \tau_{xy}}{\partial y}\right|_{j=nyp1-1} - \frac{1}{5} \cdot \left.\frac{\partial \tau_{xy}}{\partial y}\right|_{j=nyp1-2}. \tag{A5}$$

Appendix B: Sensitivity of the Results with Respect to Density and Viscosity Ratio

As the stability of the current numerical scheme depends strongly on the ratio between the liquid and the gaseous phase density and viscosity, we have performed most of our simulations with ratios of 1:10. However, realistic gas/liquid-systems typically have ratios of 1:1000, and therefore, the validity of our results was analyzed. In these simulations we used a highly efficient pressure solver (the solver PETSc,[85] using a BiCGStab method) and higher density and viscosity ratios (up to 1:100) for a Newtonian fluid. To illustrate the influence on the bubble Reynolds-number, four different cases with target Re-numbers between 0.1 and 20 were chosen (Re is a result of the simulation). The resulting deviations from the reference Reynolds number (density ratio of 1:10) are shown in Table B1. Clearly, at high Re-numbers (Re = 20) the deviation is significantly below 1%. For low Re-numbers (Re = 0.1 and Re = 1) and small density and viscosity ratios, the viscous forces are dominating inside the bubble. Here a more pronounced effect of the ratio is observed for the simulation results. This effect is in the range of about 3% and levels off quickly. Also the modified Peclet number showed a maximum sensitivity of about 3%.

Table B1. Sensitivity in % of the Re-Number with Respect to the Density and Viscosity Ratio (Reference Simulation with ρ_g/ρ_l = 1:10)

Density and Viscosity Ratio	Sensitivity (%)			
	Re = 0.1	Re = 1	Re = 5	Re = 20
1:5	−0.53	−1.05	−0.56	−0.29
1:10	0.00	0.00	0.00	0.00
1:50	2.26	2.96	0.53	0.07
1:100	2.87	3.03	0.51	0.13

In summary, our simulations with a density and viscosity ratio of 1:10 are a very good approximation of gas/liquid bubble flows, including mass transfer.

Manuscript received Jan. 19, 2007, and revision received Apr. 6, 2007.